Investigation of polarization characteristics of stable and evolutionary sub-pulse drifting in pulsars

M.Sc. Thesis

Annie Chandrika Sattenapalli



Department of Astronomy, Astrophysics and Space Engineering INDIAN INSTITUTE OF TECHNOLOGY INDORE May 20, 2025

Investigation of polarization characteristics of stable and evolutionary sub-pulse drifting in pulsars

M.Sc.Thesis

Submitted in partial fulfillment of the requirements for the awards of the degree of

Master of Science

by **Annie Chandrika Sattenapalli**



Department of Astronomy, Astrophysics and Space
Engineering
INDIAN INSTITUTE OF TECHNOLOGY INDORE
May 20, 2025

Acknowledgements

I would like to express my sincere gratitude to my supervisor, Dr. Manoneeta Chakraborty, for her continuous guidance, encouragement, and support throughout the course of this work.

I am grateful to Dr. Ramesh Bhat and Dr. Samuel McSweeny for their valuable insights and constructive discussions, which contributed significantly to this thesis. I would also like to thank Sanjay Kudale for his essential role in the Cycle 47 uGMRT data observations.

I sincerely thank my friends — Anushka, Daisy, Vishrut, Hari, Prasad, Vijay, Parth, Geetaj, Navneet, Amar, Devesh, Aryan, and Ashutosh — as well as my labmates Aromal, Jibin, and Biki, and all the faculty members, for fostering a cheerful and supportive environment, and for the many insightful and engaging discussions along the way. Last but not least, I am deeply grateful to my family for being a constant source of joy and strength, always lifting my spirits and helping me stay grounded throughout this journey.



INDIAN INSTITUTE OF TECHNOLOGY INDORE

CANDIDATE'S DECLARATION

I hereby certify that the work which is being presented in the thesis entitled **Investigation of polarization characteristics of stable and evolutionary sub-pulse drifting in pulsars** in the partial fulfillment of the requirements for the award of the degree of **MASTER OF SCIENCE** and submitted in the **DEPARTMENT OF Astronomy, Astrophysics and Space Engineering, Indian Institute of Technology Indore**, is an authentic record of my own work carried out during the time period from 24-7-2023 to 15-5-2025 under the supervision of Dr Manoneeta Chakraborty, Associate professor, DAASE, IIT Indore.

The matter presented in this thesis has not been submitted by me for the award of any other degree of this or any other institute.

13-5-2025

S. Annie Chandrika

Signature of the student with date (ANNIE CHANDRIKA SATTENAPALLI)

This is to certify that the above statement made by the candidate is correct to the best of my/our knowledge.

Marroweta Chakrakotty**
13/05/2025

Signature of the Supervisor of M.Sc. thesis (with date)
(MANONEETA CHAKRABORTY)

Annie Chandrika Sattenapalli has successfully given her M.Sc. Oral Examination held on

06-05-2025. Mansueta Chakrakosty

Signature(s) of Supervisor(s) of MSc thesis

Date: 13/05/2025

Manouesta Chakraborty Convenor, DPGC Date: 19/05/2025 Manaueta Chakrakorty Programme Coordinator, M.Sc.

Date: 19/05/2025

HoD, DAASE

Date:

Abstract

Even after decades of their discovery, pulsar emission mechanism remains an enigmatic phenomenon. Radio emission from pulsars exhibits a plethora of phenomena that modulate their pulse-to-pulse emission, observed in the form of subpulse drifting, nulling, mode changing, etc., thereby providing a range of avenues to understand the complex physical processes governing pulsar emission. Subpulse drifting is a phenomenon wherein individual substructures within the pulses march in phase across the pulse window, revealing information about the pulsar beam intricacies. Full polarimetric studies of subpulse drifting, though challenging and hence limited, can, in principle, shed light on the 'spark' geometry and its evolution required to explain this phenomenon.

PSR J0026–1955 is a newly discovered pulsar, which has been observed to exhibit highly peculiar subpulse drifting behavior, including mode switching It also exhibits a high nulling fraction of approximately 58%. Our study presents the first polarization analysis of the subpulse drifting behavior in this pulsar utilizing the high-sensitivity full polarimetric data from the upgraded Giant Meterwave Radio Telescope (uGMRT). In this investigation, we focus on the subpulse drifting in full polarimetric mode, orthogonal polarization mode (OPM) switching, and drift-synchronous polarization modulation. We examine the polarization properties and associated parameters and compare their evolution over the various subpulse drifting modes, and in particular, we compare the stable and evolutionary drift modes.

Our work has revealed notable changes in the polarization angle (PA) at peak longitude, supporting the rotating vector model proposed by Radhakrishnan and Cooke. Observations of drift rate changes suggest the dominance of the evolutionary modes, which are transient (short-lasting) compared to the stable drifting modes. Using the Stokes parameters and derived polarization plots, we have identified synchronous drift modulation of the position angle, alongside periodic behaviour in ellipticity angle plots and circular polarisation Plots. We analyzed the averaged position angle (PA) curve for modes A0 and B. Mode A0 displayed a shallower slope, while mode B exhibited a steeper slope. This observation supports the nested carousel model, which suggests that B modes originate from sparks closer to the magnetic axis, whereas A0 modes are generated by sparks located farther away. Additionally, our examination of the ellipticity angle plots for both A0 and B modes indicates that the behavior is more circular in mode B compared to mode A0. This suggests that regions closer to the magnetic axis exhibit greater circularity, while circularity in polarisation diminishes as we move away from the magnetic axis.

Contents

List of Figures

List of Tables

1	Intr	oductio	n	1
	1.1	Pulsar	s	1
		1.1.1	What are Pulsars?	1
		1.1.2	Discovery	1
		1.1.3	Observation of Pulsars	1
		1.1.4	Radio emission	3
		1.1.5	Sub-pulse Drifting	4
		1.1.6	Drift Rate	4
	1.2	Polariz	zation Perspective	6
		1.2.1	Stokes Parameters	8
		1.2.2	Polarisation Parameters	8
		1.2.3	Rotating Vector Model-RVM	9
		1.2.4	Drift-Synchronous Modulation of Polarization	10
		1.2.5	Previous Polarisation studies	10
	1.3	Resear	ch Objectives	11
	1.4	PSR J	0026-1955	12
2	Inst	rument		13
	2.1	The up	ograded Giant Meterwave Radio Telescope (uGMRT)	13
	2.2	Observ	vations	14
		2.2.1	Cycle-41 and cycle-47 technical details	14
		2.2.2	In-field Phasing	16
3	Ana	lysis an	d Results	18
	3.1	Prilim	inary Analysis	19
		3.1.1	Data Reduction	19

5	Future dire	ctions	61
4	Discussion		58
	3.1.7	Stokes Representation of interesting features	50
	3.1.6	Polarimetric view of the four subpulse drifting modes	34
	3.1.5	Interesting Drifting Features	32
	3.1.4	Drift Band Fitting	26
	3.1.3	Longitude-Resolved Fluctuation Spectrum (LRFS)	25
	3.1.2	Averaged Polarization Profile	22

List of Figures

1.1	Pulsars Are Rapidly Spinning Neutron Stars. The blue curved lines represent	
	the magnetic field lines, emanating from the neutron star's magnetic poles.	
	The yellow lines depict the beams of electromagnetic radiation emerging from	
	the magnetic poles. The magnetic axis is tilted with the rotation axis, an	
	arrangement without which the pulses do not appear. CREDIT: Bill Saxton,	
	NRAO/AUI/NSF	2
1.2	Prof. Jocelyn Bell's First Pulsar with Chart Recordings, Credit: CSIRO	3
1.3	Image showing a Subpulse drifting plot. The x-axis represents pulse longitude,	
	while the y-axis the pulse number. P2: Distance between subpulses; P3: Time	
	for subpulse phase repetition	5
1.4	Illustration of the RVM, showing how the polarisation angle (PA) changes as the	
	observer's line of sight passes through the pulsar's magnetic field lines. Arrows	
	represent the emitted radiation direction, and dashed lines indicate the magnetic	
	field structure. Credits: Crispin Agar	9
1.5	The pulsar geometry diagram shows the rotation axis (Ω) , magnetic axis (B) ,	
	and the observer's line of sight. α and β control the PA sweep, which becomes	
	more abrupt as the line of sight nears the magnetic pole, with a rapid swing	
	from +45° to -45°. Credits: Crispin Agar	9
1.6	Modelled S-shaped polarisation position angle (PA) swing expected from the	
	RVM, varying smoothly across pulse longitude	9
2.1	uGMRT, Pune. Credit: NCRA, TIFR	13
3.1	Comparison of uncleaned (left column) and cleaned (right column) data: Frequency	-
	phase plots, integrated profiles, and driftband clarity across 120 pulses	21
3.2	Observation cycle-37: Average Profile in total (black), linear (red), and circular	
	polarisation (blue) vs longitude.	23
3.3	Observation cycle 47: Average Profile in total (black), linear (red), and circular	
	polarization (blue) vs longitude	23

cycle-47 Observation: Top: The longitude averaged position angle (PA) curve of linear polarisation across pulse longitude. The PA is calculated using the relation PA = $\frac{1}{2} \tan^{-1} \left(\frac{U}{Q} \right)$, which describes the orientation of the linear polarisation vector. Bottom: The circular contribution angle $\theta = \tan^{-1} \left(\frac{V}{L} \right)$, where	
$L = \sqrt{Q^2 + U^2}$, characterizes the relative dominance of circular to linear polarisation. Higher values of θ indicate stronger circular polarisation contributions.	24
cycle-47 Observation: LRFS. Bottom: Integrated pulse profile. Longitude-Resolved Fluctuation Spectrum (LRFS) showing a peak near 0.04 cycles per rotation, indicating an average subpulse repetition period (P_3) of approximately 25 pulses	25
Modes A0 and B. The black lines illustrate the quadratic fits, while the green crosses denote the subpulse peaks. The software utilizes these green crosses to apply linear and quadratic models, effectively representing the drift bands	27
Modes A1 and A2. The black curves illustrate the quadratic fits, while the green crosses denote the subpulse peaks. The software utilizes these green crosses to apply linear and quadratic models, effectively representing the drift bands	28
Drift Rate Distributions by Mode: Histograms of subpulse drift rates for different drift modes	30
Histogram of drift rate distribution: X-axis for drift rate, Y-axis for occurrences.	30
P_3 as a function of pulse number. Constant P_3 value indicates stable drift modes A0 and B; increasing P_3 indicates A1 mode; and decreasing P_3 indicates A2 modes in the pulse numbers	31
Drift rate as a function of pulse number. A constant drift rate indicates stable drift modes, while increasing and decreasing drift rates represent slow-to-fast and fast-to-slow drift modes, respectively. The negative sign indicates the peak is shifting earlier in phase compared to the last period	31
Illustration of gradual drift mode transitions and switching between different drift states	33
Illustration of Nulling, rapid drift mode transitions and switching between different drift states	34
Cycle-41 observation: Smoothed Stokes Parameters (I, Q, U, V): This panel displays the Gaussian-smoothed Stokes parameters across pulse number and pulse longitude within the window 110–170. Each subpanel corresponds to one of the Stokes components, highlighting the intensity and polarization structure of the emission. Gaussian smoothing with $\sigma = 1.5$ enhances coherent features while suppressing noise	37
	of linear polarisation across pulse longitude. The PA is calculated using the relation PA = $\frac{1}{2} \tan^{-1} \left(\frac{U}{Q} \right)$, which describes the orientation of the linear polarisation vector. Bottom: The circular contribution angle $\theta = \tan^{-1} \left(\frac{V}{L} \right)$, where $L = \sqrt{Q^2 + U^2}$, characterizes the relative dominance of circular to linear polarisation. Higher values of θ indicate stronger circular polarisation contributions. cycle-47 Observation: LRFS. Bottom: Integrated pulse profile. Longitude-Resolved Fluctuation Spectrum (LRFS) showing a peak near 0.04 cycles per rotation, indicating an average subpulse repetition period (P_3) of approximately 25 pulses

3.15	Cycle-41 observation: Derived Polarization Quantities: This panel shows polariza-	
	tion metrics derived from smoothed Stokes parameters. The ellipticity angle (EA) and	
	position angle (PA) trace the geometry of the polarization, while the fractional linear	
	(L) and fractional circular (C) polarizations quantify the strength of linear and circular	
	components relative to total intensity	38
3.16	Cycle-47 observation: Smoothed Stokes Parameters (I, Q, U, V): This panel displays	
	the Gaussian-smoothed Stokes parameters across pulse number and pulse longitude	
	within the window 270-310. Each subpanel corresponds to one of the Stokes compo-	
	nents, highlighting the intensity and polarization structure of the emission. Gaussian	
	smoothing with σ = 1.5 enhances coherent features while suppressing noise	39
3.17	Cycle-47 observation: Derived Polarization Quantities: This panel shows polariza-	
	tion metrics derived from smoothed Stokes parameters. The ellipticity angle (EA) and	
	position angle (PA) trace the geometry of the polarization, while the fractional linear	
	(L) and fractional circular (C) polarizations quantify the strength of linear and circular	
	components relative to total intensity	40
3.18	I, Q, U, V plots for Mode A0: This figure shows the Stokes parameters for Mode	
	A0. The total intensity (I), linear polarization components (Q and U), and circular	
	polarization (V) are plotted across pulse phase to analyze polarization behavior in this	
	mode	41
3.19	I, Q, U, V plots for Mode B: The Stokes parameters for Mode B are shown, capturing	
	the mode-dependent polarization structure across pulse longitude. The variations in Q,	
	U, and V highlight changes in polarization geometry	42
3.20	I, Q, U, V plots for Mode A1: Polarization profiles for Mode A1, illustrating the	
	behavior of intensity and polarization components across the pulse. These help identify	
	distinguishing polarization patterns for this mode	43
3.21	I, Q, U, V plots for Mode A2: This figure presents the Stokes profiles for Mode A2,	
	showing the temporal evolution and polarization characteristics of this drift mode	44
3.22	Derived polarisation quantities for Mode A0	46
3.23	Derived polarisation quantities for Mode B	47
3.24	Derived polarisation quantities for Mode A1	48
3.25	Derived polarisation quantities for Mode A2	49
3.26	Switch between modes A and B. Lower half drifts slow \rightarrow fast, upper half fast \rightarrow slow.	52
3.27	Gradual drift mode transitions and switching between different drift states in Stokes	
	representation. $A0 \rightarrow A2 \rightarrow Null \rightarrow A1 \rightarrow A0$	53
3.28	Nulls between the drift bands B in Stokes representation. Memory across nulls along	
	drift bands is noted	54

3.29	Sudden drift mode transitions between different drift states (A0 to B) in Stokes repre-	
	sentation	55
3.30	Mean Stokes profiles (I, Q, U, and V) across pulse longitude after pulse averaging	
	and rolling mean smoothing within the window $270^{\circ}-320^{\circ}$	56
3.31	Comparison of position and ellipticity angle profiles for drift modes A0 and B.	57

List of Tables

2.1	Frequency bands of uGMRT. Current observation is conducted in Band 3	13
2.2	Technical details of Cycle 41 uGMRT observations for PSR J0026–1955	14
23	Technical details of Cycle 47 uCMPT observations for DSD 10026, 1055	15

Chapter 1

Introduction

1.1 Pulsars

1.1.1 What are Pulsars?

Pulsars are highly magnetised, rotating neutron stars emitting electromagnetic radiation beams along their magnetic axis. These stars are the remnants of massive stars that exploded in supernovae, leaving behind incredibly dense, compact stars that rotate at extremely high speeds, with periods ranging from milliseconds to seconds. Their magnetic fields typically range from 10^8 to 10^{13} Gauss (Gold 1969), making them some of the most highly magnetised objects in the universe. As these stars rotate, beams of radiation from these stars sweep across our line of sight, which we perceive as pulsation (similar to beams observed from a lighthouse). An artist's representation of such a pulsar is shown in Figure 1.1.

1.1.2 Discovery

The discovery of pulsars occurred in 1967 (Hewish et al. 1968) by *Jocelyn Bell Burnell* and *Antony Hewish*, Figure 1.2. They detected regular radio pulses emanating from a certain direction in the sky, observed as a scruffy pattern on the chart recorder. The astonishing regularity of the patterns initially made them think they were from "Little Green Men" (LGM). Further analysis revealed that these signals were coming from a rapidly rotating neutron star, now known as the first pulsar, PSR B1919+21.

1.1.3 Observation of Pulsars

Pulsars are generally detected through their periodic electromagnetic radiation, which is observable across various wavelengths, including

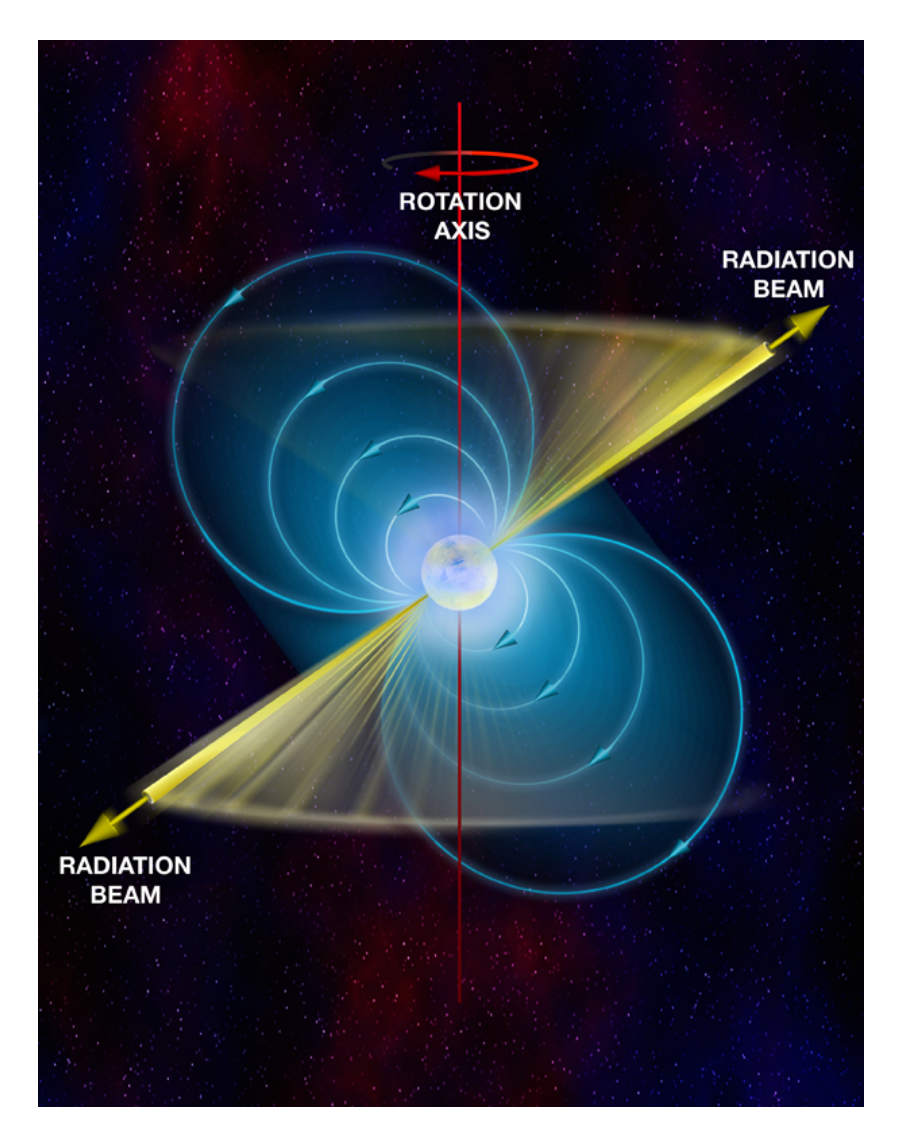


Figure 1.1: Pulsars Are Rapidly Spinning Neutron Stars. The blue curved lines represent the magnetic field lines, emanating from the neutron star's magnetic poles. The yellow lines depict the beams of electromagnetic radiation emerging from the magnetic poles. The magnetic axis is tilted with the rotation axis, an arrangement without which the pulses do not appear. CREDIT: Bill Saxton, NRAO/AUI/NSF

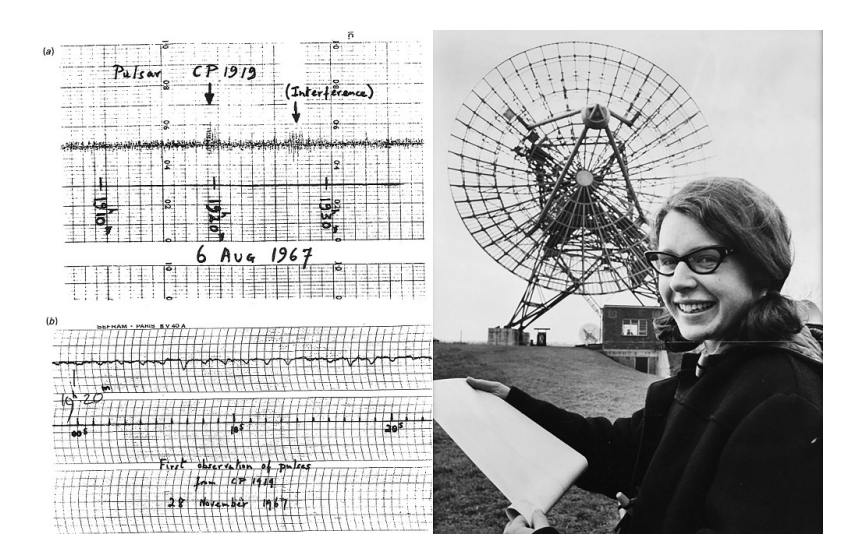


Figure 1.2: Prof. Jocelyn Bell's First Pulsar with Chart Recordings, Credit: CSIRO.

radio, X-ray, and gamma-ray bands. They look like a lighthouse flickering on and off as the beams face towards and away from our line of sight. The most prevalent method for identifying pulsars involves using radio telescopes, which can capture their consistent radio pulses. They capture these signals by measuring the intensity as a function of time, which shows regular periodic peaks. These pulses are observed to have a precision far exceeding a millionth of a second, and oftentimes, reaching to a billionth of a second (or even better), which means they can be used as extremely accurate celestial clocks.

1.1.4 Radio emission

Pulsars can be likened to enormous dynamos. When a pulsar forms from a supernova explosion, it has a high spin and a strong magnetic field due to the conservation of angular momentum and magnetic flux. The dynamo effect comes into play by inducing electric potentials that arrange charges on the surface in a way that counteracts the impact of the electric potential (Goldreich and Julian 1969).

On the surface of the star, these charges are rapidly pulled by strong electric fields and they suddenly encounter a powerful magnetic field component as they are pulled away from the surface. The magnetic field at the surface is so strong that the charged particles are forced to move along the magnetic field lines (known as the $E \times B$ effect), similar to beads sliding along a string (Radhakrishnan and Cooke 1969).

As charged particles travel along the curved magnetic field lines of a pulsar, they emit curvature radiation—a process resulting from their acceleration along these paths. As these high-energy photons propagate outward from the pulsar surface, they may encounter strong magnetic fields where they interact to produce electron-positron pairs. These secondary particles, being charged and also constrained to move along the curved field lines, emit additional—though weaker—curvature radiation. As the altitude above the pulsar increases, this cascading process leads to progressively less energetic radiation, since each generation of particles produces weaker emissions.

1.1.5 Sub-pulse Drifting

Subpulse drifting in pulsars refers to the phenomenon where the individual subpulses (complex structures within the main pulse) shift systematically in phase over time, as shown in Figure 1.3. This drifting is observed as a periodic or quasi-periodic movement of the subpulses within the pulse window (Drake and Craft 1968). This drift is often characterised by two key parameters:

- *P*₂ (**Separation between subpulses**): The horizontal distance between successive subpulses in the pulse profile.
- P_3 (**Drift period**): The time it takes for a subpulse to reappear at the same phase position. This factor helps us characterise and differentiate different modes in the pulse stack. The units of P_3 are generally in pulsar rotations.

1.1.6 Drift Rate

The drift rate, D, is defined as:

$$D = \frac{\Delta \phi}{P_1} \quad \left(\frac{\circ}{P_1}\right)$$

where D is the drift rate in degrees per pulse period, $\Delta \phi$ represents the longitude shift in degrees over one pulse period, and P_1 is the pulse period.

The **carousel model** (Ruderman 1975) explains subpulse drifting as the rotation of sub-beams around the magnetic axis of the pulsar. In this model, these sub-beams are formed from sparks near the surface of the

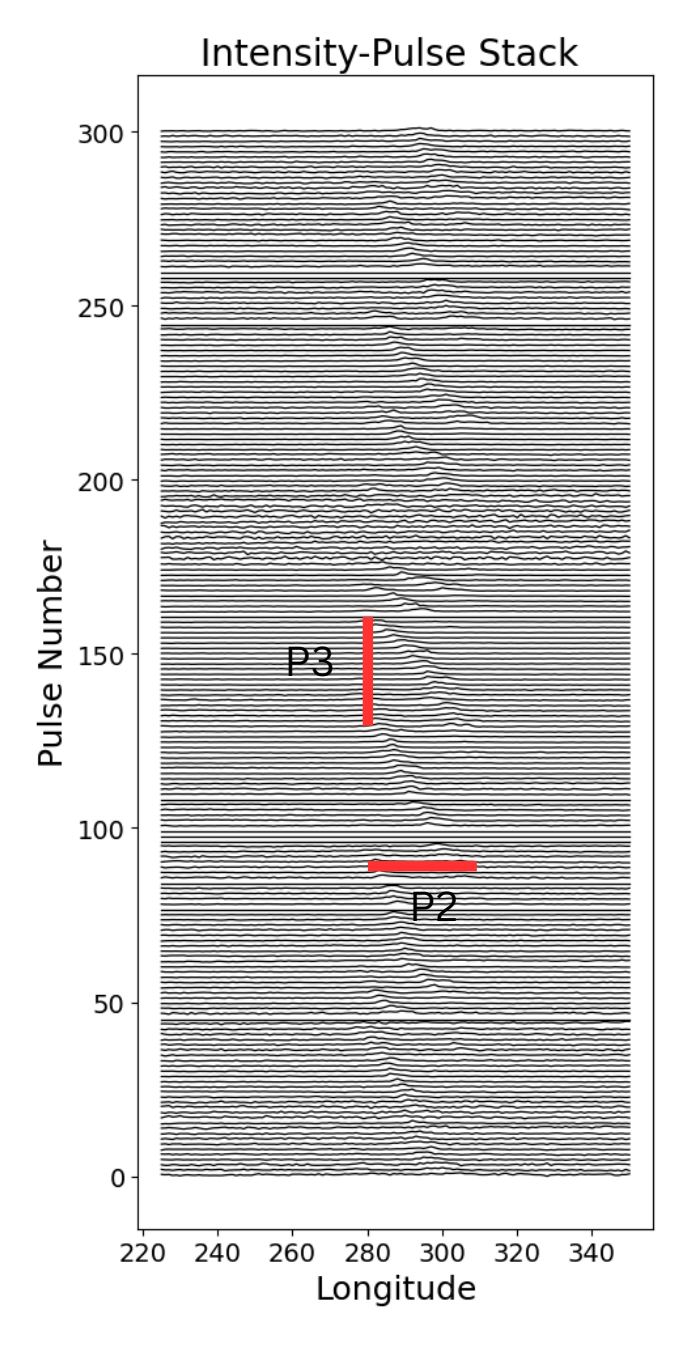


Figure 1.3: Image showing a Subpulse drifting plot. The x-axis represents pulse longitude, while the y-axis the pulse number. P2: Distance between subpulses; P3: Time for subpulse phase repetition.

pulsar around the magnetic axis and rotate around the magnetic axis with a period of P_4 . However, it does not account for several key phenomena that are observed in pulsars. These include **drift rate variability**, where the subpulse drift rate changes over time; **mode switching**, where pulsars transition between different drifting patterns; **evolutionary drifting**, where the drifting pattern smoothly evolves with time; **nulling**, which is the temporary cessation of emission; and **frequency-dependent polarization modulation**, where the polarization properties of the emission vary with frequency.

Within a pulse stack, the space between the drift bands shows how a subpulse comes back at a certain time (P_3) . We can only see the position of subpulses once for each pulse. It can be hard to track a subpulse from one pulse to the next because of aliasing effects. This makes it tricky to know how fast the carousel beams are moving. Sometimes, this aliasing can make the drift rate look different, even if nothing has changed. The presence of multiple drift rates in a pulsar may indicate, or at least suggest, a change in the number of sub-beams responsible for the drifting emission pattern(Rankin, Wright, and Brown 2013; S. McSweeney et al. 2017; Janagal et al. 2023)

1.2 Polarization Perspective

Polarization refers to the orientation of the electric field vector in an electromagnetic wave. In astrophysical contexts, such as pulsars, polarization provides important insights into the geometry and physical processes of emission.

When a charged particle accelerates—particularly in the presence of a magnetic field—it emits electromagnetic radiation. This radiation is often polarized due to the motion of the particle and the influence of the magnetic field.

The intensity of radiation emitted by an accelerating charge is described by the Larmor formula, which quantifies the total power radiated:

$$P = \frac{q^2 a^2}{6\pi\varepsilon_0 c^3} \tag{1.1}$$

where q is the charge of the particle, a is the acceleration, ε_0 is the vacuum permittivity, and c is the speed of light.

If the particle moves relativistically in a magnetic field, it follows a

spiral trajectory due to the Lorentz force:

$$\mathbf{F} = q(\mathbf{v} \times \mathbf{B}) \tag{1.2}$$

This motion results in *synchrotron radiation*, which is highly polarized. The emitted radiation is primarily perpendicular to the acceleration direction, leading to a preferred polarization direction.

The observed polarization depends on the angle θ between the observer and the particle's velocity:

- At " $\alpha = 90^{\circ}$ " (perpendicular to motion): Radiation is strongly linearly polarized.
- At other angles: A mix of linear and circular polarization occurs.
- At $\alpha=0^\circ$ or 180° (parallel to motion): Little or no polarization is observed.

1.2.1 Stokes Parameters

The polarization state can be described using Stokes parameters:

$$I$$
 = Total intensity $U = I_{45^{\circ}} - I_{-45^{\circ}}$
 $Q = I_x - I_y$ $V = I_R - I_L$ (1.3)

where I_x , I_y represent intensities along the horizontal and vertical axes, and I_R , I_L correspond to the right- and left-circular polarization.

Circular polarization occurs when two perpendicular linearly polarized waves have equal amplitudes and a phase difference of 90°:

For a charged particle spiraling around a magnetic field line:

- A combination of linear and circular polarization is seen when viewed at an oblique angle.
- Right and left circular polarization depend on whether the electric field vector rotates clockwise or counterclockwise, as seen by the observer.

1.2.2 Polarisation Parameters

• Ellipticity Angle (χ) :

$$\chi = \frac{1}{2} \tan^{-1} \left(\frac{V}{\sqrt{Q^2 + U^2}} \right)$$

It ranges from -45° to 45° — 0° means the polarization is purely linear, while $\pm 45^{\circ}$ indicates circular polarization.

• Position Angle (ψ) :

$$\psi = \frac{1}{2} \tan^{-1} \left(\frac{U}{Q} \right)$$

The position angle ranges from -90° to $+90^{\circ}$. It represents the orientation of the pulsar's magnetic field relative to the celestial North.

• Fractional Linear Polarisation:

$$\frac{L}{I} = \frac{\sqrt{Q^2 + U^2}}{I}$$

• Fractional Circular Polarization:

$$\frac{V}{I}$$

1.2.3 Rotating Vector Model-RVM

The **Rotating Vector Model (RVM)** explains how the *position angle* gradually changes as a pulsar rotates. As the pulsar spins, we receive radiation from different regions of its magnetic field (Figure 1.4). This results in the polarisation angle shifting smoothly throughout the pulse, often seen as an S-shape curve (see Figure 1.6. (Radhakrishnan and Cooke 1969

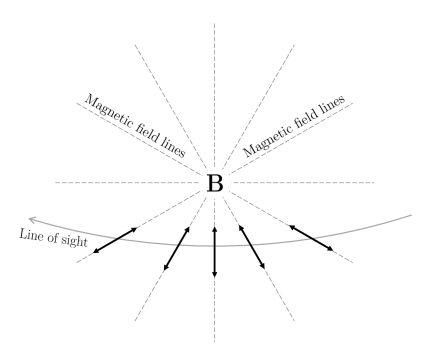


Figure 1.4: Illustration of the RVM, showing how the polarisation angle (PA) changes as the observer's line of sight passes through the pulsar's magnetic field lines. Arrows represent the emitted radiation direction, and dashed lines indicate the magnetic field structure. Credits: Crispin Agar.

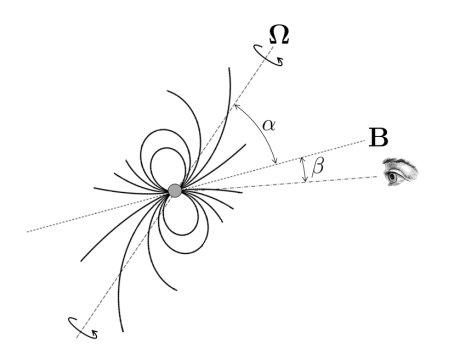


Figure 1.5: The pulsar geometry diagram shows the rotation axis (Ω) , magnetic axis (B), and the observer's line of sight. α and β control the PA sweep, which becomes more abrupt as the line of sight nears the magnetic pole, with a rapid swing from +45° to -45°. **Credits: Crispin Agar.**

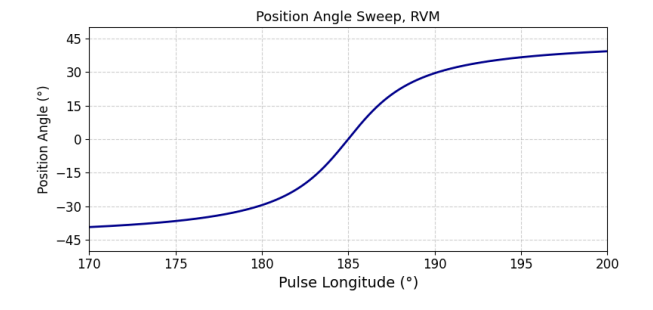


Figure 1.6: Modelled S-shaped polarisation position angle (PA) swing expected from the RVM, varying smoothly across pulse longitude.

1.2.4 Drift-Synchronous Modulation of Polarization

Drift-synchronous modulation refers to the periodic variation of polarization properties due to drifting subpulses in pulsars. The polarisation properties mimic the drifts with gradual transition along the longitudes and pulse number. The key effects include:

- **Periodic changes in linear and circular polarization:** The polarization state varies periodically, matching the subpulse drift cycle.
- **Rotation of the Polarization Angle:** The position angle of the polarized light follows a structured pattern associated with the drifting subpulses.
- **Dependence on Viewing Geometry:** The observer's line of sight determines how the periodic polarization changes are perceived.

Observations of drift-synchronous modulation provide insights into plasma dynamics in strong magnetic fields.

1.2.5 Previous Polarisation studies

There have been only a limited number of previous studies, like those of Ramachandran et al. 2002; Primak et al. 2022 and Oswald, Karastergiou, and Johnston 2023 and they have progressively deepened our understanding of pulsar polarization and subpulse behaviour. Ramachandran et al. 2002 challenged early claims about subpulse polarization angle rotation by demonstrating that such apparent rotations in pulsars like B0809+74 and B2303+30 are instead due to abrupt switching between two orthogonal polarization modes. Their findings support the idea that pulsar radiation largely conforms to the rotating vector model (RVM) when modal effects are properly considered Ramachandran et al. 2002. Edwards 2004 studied the polarization behaviour of drifting subpulses in pulsars using a technique based on the polarimetric fluctuation spectrum, revealing complex patterns beyond simple orthogonal polarization modes.

Building on this, N. Primak et al. 2022 conducted a detailed polarization analysis of PSR B1919+21. They discovered a toroidal distribution of polarization vectors in Poincaré space, synchronized with subpulse drifting. This circular modulation in polarization is not accounted for by standard models, suggesting a need for new theoretical interpretations,

potentially involving coherent or partially coherent mode interactions. Oswald, Karastergiou, and Johnston 2023 attempt to address this gap by introducing a partial-coherence model, showing that many complex polarisation features (including circular polarisation and RVM departures) can be explained by varying the coherence and phase relationship between orthogonal modes. Their model provides a unifying framework for both individual and population-level polarisation behaviour in pulsars.

1.3 Research Objectives

In the past, several studies have been conducted on the polarisation features of integrated profiles. However, due to limitations in telescope sensitivity, the analysis of individual pulses has been fairly limited, particularly those pertaining to drifting subpulses. This project therefore will focus on the single pulse analysis of drifting subpulses. It examines the polarisation features and variations across different pulse numbers and longitudes for various subpulse drift rates and P_3 values (the parameters that categorise them into different modes). It can provide insights into beam geometry and emission mechanisms related to different drift modes.

Using the upgraded Giant Meterwave Radio Telescope (uGMRT), we will investigate subpulse drifting in the pulsar PSR J0026–1955, which is known to show multiple drift modes, various drift modes, as well as a multitude of other curious features such as long-duration nulls, and drift-null connections. Our objective is to conduct an in-depth analysis of polarisation features with drift patterns, examining how these characteristics change with pulse longitude and drift modes in order to enhance our understanding of pulsar emissions through Stokes parameters.

The main goals of this study are as follows:

- 1. Classification of various drift modes for the PSR J0026–1955.
- 2. Investigate Stokes parameters: I (total intensity), Q (linear polarization aligned along 0° and 90°), U (linear polarization aligned along $+45^{\circ}$ and -45°), and V (circular polarization), across different emission modes.
- 3. Investigate derived parameters like the ellipticity angle, PA, fractional linear and fractional circular polarization.

4. Investigate gradual transitions between stable and evolutionary modes, along with nulls and rapid mode switching, using polarization analysis with Stokes parameters.

1.4 PSR J0026-1955

The Murchison Widefield Array (MWA) independently discovered PSR J0026–1955 in its ongoing Southern-Sky MWA Rapid Two-metre (SMART) pulsar survey Samuel J McSweeney et al. 2022; N. Bhat et al. 2023. It turns out the pulsar was initially listed as a candidate in the Green Bank Northern Celestial Cap (GBNCC) pulsar survey Stovall et al. 2014. The analysis of SMART data revealed that the pulsar exhibits subpulse drifting in remarkable ways, as well as a large nulling fraction of ~ 77 per cent, along with drift rate evolution, and rapid mode changing. This makes the pulsar an excellent object to scrutinize the carousel model. A more recent study by Janagal et al. 2023, which is also the first detailed study of this pulsar using the uGMRT, discusses the identification of four distinct subpulse drifting modes: A0, A1, A2 and B, in the full intensity mode at 300-500 MHz.

Chapter 2

Instrument

2.1 The upgraded Giant Meterwave Radio Telescope (uGMRT)

The upgraded Giant Meterwave Radio Telescope (uGMRT)is located in Pune, India. The legacy system (GMRT) was operational since 2001 and following a major upgrade in 2017, the telescope has been referred to as uGMRT. It operates between 150 MHz and 1450 MHz, capturing various phenomena in space like pulsars and cosmic background radiation.



Figure 2.1: uGMRT, Pune. Credit: NCRA, TIFR

Name	Frequency range
Band 2	130-260 MHz
Band 3	250-500 MHz
Band 4	550-900 MHz
Band 5	1000-1450 MHz

Table 2.1: Frequency bands of uGMRT. Current observation is conducted in Band 3.

The uGMRT consists of 30 antennas, each 45 meters in diameter, spread

over a distance of 25 km. This configuration provides exceptional sensitivity and high fidelity for sharp imaging at frequencies below 1 GHz, making it ideal for studying faint radio signals. Additionally, it is capable of performing full polarimetric observations, allowing pulsar and low-frequency researchers to analyse the detailed emission mechanisms of radio-frequency emitting sources . uGMRT can also be used as a phased array, where sensitive, pointed beams can be formed and steered. This works by the combination of several individual elements (antennas) of the telescope acting as an interferometer. This electronic steering of beams is achieved by adjusting for the phase of the signal received by each antenna in the array. Then it combines the signals coherently such that it focuses the receiving beam in desired directions in the sky.

The substantial sensitivity improvements of the uGMRT now enable systematic single-pulse analysis for a wide range of pulsars. This improvement is critical for probing pulse-to-pulse variability, subpulse drifting, nulling behavior, and mode switching phenomena in much greater detail than that has been possible before

2.2 Observations

2.2.1 Cycle-41 and cycle-47 technical details

Parameter	Details
Target	PSR J0026–1955
Observation Band	Band 3 (300–500 MHz), Band 4 (550–750
	MHz)
Observation Mode	Phased Array
Technique	Standard Phasing
Data Used	Only Band 3 (Band 4 affected by strong RFI)
Number of Channels	2048 channels, 200 MHz bandwidth
Frequency Resolution	97.65 kHz
Time Resolution	655.56 μs

Table 2.2: Technical details of Cycle 41 uGMRT observations for PSR J0026–1955.

To gain deeper insights into the atypical characteristics displayed by this pulsar, additional observations were proposed and successfully obtained, alongside the previous data worked on by Janagal et al. 2023. The details are given below.

Parameter	Details
Target	PSR J0026–1955
Observation Band	Band 3 (300–500 MHz)
Observation Mode	Phased Array
Technique	Infield Phasing
Data Used	Band 3 only
Number of Channels	2048 channels, 200 MHz bandwidth
Frequency Resolution	97.65 kHz
Time Resolution	655.56 μs
Total Observation Time	10 hours

Table 2.3: Technical details of Cycle 47 uGMRT observations for PSR J0026–1955.

2.2.2 In-field Phasing

We employed a novel technique known as in-field phasing for the Cycle-47 data collection. In radio interferometry, antenna arrays are used to observe faint astronomical sources by combining their signals coherently. For this to work effectively, the signals received at each antenna must be kept in phase. This process is called *phasing*, and it ensures that the combined signal is maximally constructive, improving both sensitivity and resolution. The details of this new method, including the conceptual framework and validation are described in Sanjay Kudale et al. 2024

Conventional Phasing Method

Traditionally, phase corrections are determined using an external calibrator — a bright, well-characterised source located near our target in the sky. Observations of this calibrator are used to estimate the phase and amplitude errors at each antenna. These solutions are then applied during the observation of the actual target.

However, this approach presents several limitations:

- The ionosphere introduces time-varying phase errors, which can evolve on timescales shorter than the typical 30–40 minute calibration cycle.
- Antennas with long baselines (i.e., far from the core) are more affected by phase errors and are often excluded to maintain coherence, reducing sensitivity.
- Switching to a calibrator interrupts the science observation, disturbing long, continuous monitoring tasks.

Concept of In-field Phasing

In-field phasing addresses these challenges by performing phase calibration using the target field itself. Instead of relying on an external calibrator, this method:

- Utilizes a model of the target field derived from previous imaging observations.
- Continuously compares real-time interferometric data with the predicted model visibilities.

 Derives and applies antenna-based phase corrections during the observation, without interruption.

At the upgraded GMRT (uGMRT)(Gupta et al. 2017), this method is implemented in the GMRT Wide-Band backend (GWB)(Reddy et al. 2017, which supports rapid updates of phase solutions (every 1–2 minutes). The process is conceptually similar to self-calibration in imaging, but applied in real-time and tailored for beamforming.

Advantages of In-field Phasing

This technique offers several key benefits:

- **Uninterrupted Observations:** Allows for continuous data acquisition without external calibration.
- **Increased Sensitivity:** Coherent combination of all antennas, including those with long baselines is possible.
- Real-time Adaptability: Frequent phase corrections to adjust for rapid atmospheric changes.
- Improved Data Quality: Boosts signal-to-noise ratio for precise measurements of pulsar dispersion measures and timing.

Chapter 3

Analysis and Results

We conducted a detailed single-pulse analysis including polarimetric studies of the pulsar PSR J0026–1955 using data taken during the cycle 41 and cycle 47 of uGMRT. The observation of this pulsar was made in Band 3 in the filterbank format, where the pulse intensity with time and frequency is recorded in full Stokes. Using the dspsr software (van Straten & Bailes 2011), the data were de-dispersed (correcting for the effects due to propagation in the interstellar medium) and converted into the timer archive format. These archive files contain the single pulse information for each pulse and the corresponding polarization parameter values.

To begin with, we used the data previously obtained by our group that was also reported in Janagal et al. 2023. Following that, the data acquired during November 2024 were also analysed. The data were de-dispersed (processed to correct for dispersion measure), followed by an initial RFI (radio frequency interference) cleaning and full frequency scrunching, collapsing all 2048 frequency channels into a single time series. In the full-intensity Stokes mode (*I*), the single pulse stack was plotted using PSRCHIVE software (Hotan et al. 2004; van Straten et al. 2012), revealing the presence of RFI. Subsequent RFI cleaning produced high fidelity single-pulse stacks in each of the Stokes modes. The averaged polarization profiles and associated position angle (PA) variations were generated using PSRCHIVE, after the cleaning of the data.

3.1 Priliminary Analysis

3.1.1 Data Reduction

We performed further analysis using selected 10-minute and 30-minute segments from the Cycle 41 observation. These segments exhibit high signal-to-noise ratio (SNR) pulse stacks containing distinct drift modes, including periods of nulling, allowing maximum feature identification within localised windows. Standard pulsar data reduction techniques were applied, including RFI zapping using PSRCHIVE's interactive pazi tool.

We conducted two observations with the uGMRT in Band 3 during Cycle 47. Although the second observation slot was originally intended for Band 4, prevailing scintillation conditions made successful Band 4 observations highly unlikely. Consequently, the second observation was also carried out in Band 3.

The filterbank format data were processed using dspsr to apply dispersion measure (DM) corrections (i.e. de-dispersion) and generate folded single-pulse archives. After initial processing, a total of 10,630 individual pulses were extracted for analysis.. These pulses were divided into 11 batches for subsequent analysis. Rotation measure (RM) corrections were also applied to each batch to account for Faraday rotation caused by the interstellar medium.

Following RM correction, the data were transformed into the frequency domain, where RFI was mitigated by identifying and excising contaminated frequency channels ("zapping"). Each batch was then examined for the presence of organized subpulse drift bands.

Out of the 11 batches analyzed, only 3 exhibited clear drift band structures after RFI mitigation. These driftband-containing batches were subsequently combined for further pulse zapping using the PAZI tool to remove individual corrupted pulses. After pulse-level zapping, the cleaned archive files were frequency-scrunched and converted into ASCII format for detailed drift rate and subpulse analysis.

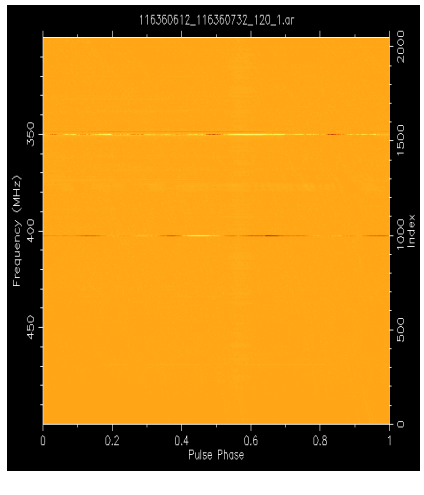
However, the zapped pulse information from pazi could not be directly preserved in a format compatible with downstream processing.

To address this, the zapped pulse numbers were recorded, and a custom script was developed to replace their full polarimetric information with null values. This ensured data compatibility while maintaining the RFI mitigation across the dataset.

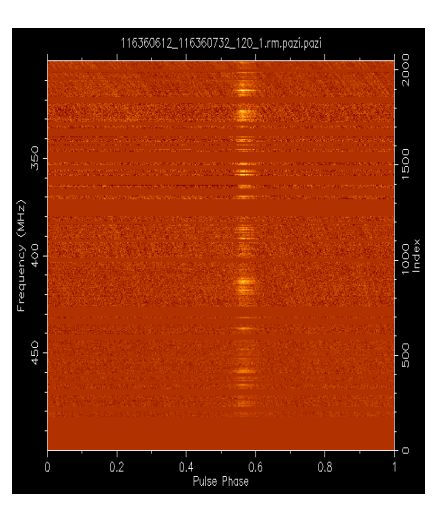
Figures 3.1a and 3.1b compare the frequency vs. phase plots before and after cleaning, where the left column (Figure 3.1a) shows a cluttered frequency-phase space due to the presence of noise, while the right column (Figure 3.1b) illustrates the improved clarity after cleaning, with noise and unwanted components removed.

Figures 3.1c and 3.1d display the integrated pulse profiles before and after the cleaning process. In the left column (Figure 3.1c), the profile appears distorted due to RFI contamination, whereas the right column (Figure 3.1d) shows a much cleaner, cleaner pulse profile post-cleaning.

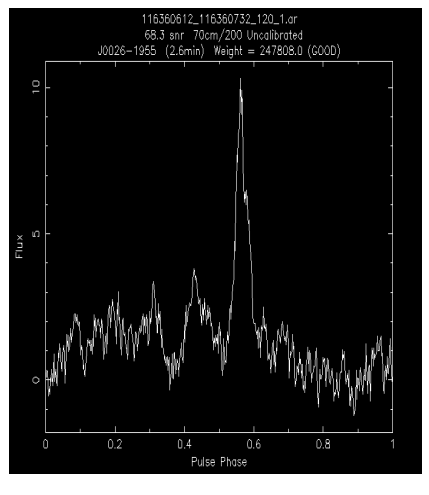
Figures 3.1e and 3.1f highlight the impact of RFI on the driftband structures. In Figure 3.1e (left), RFI severely obstructs the driftbands, making them difficult to distinguish. In contrast, Figure 3.1f (right) shows the driftbands clearly visible after cleaning, demonstrating the effectiveness of the RFI cleaning process in recovering the driftband structures.



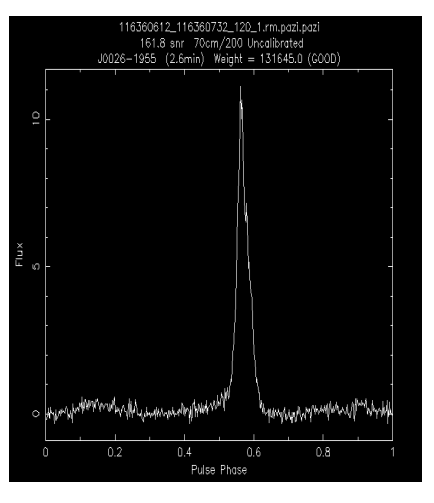
(a) Frequency vs. phase (before cleaning, 2480 frequency bins)



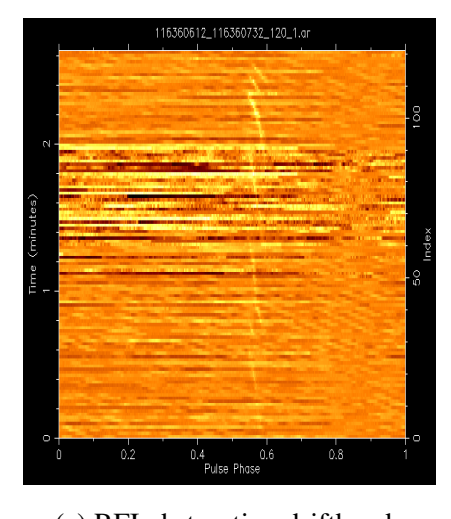
(b) Frequency vs. phase (after cleaning, 2480 frequency bins)



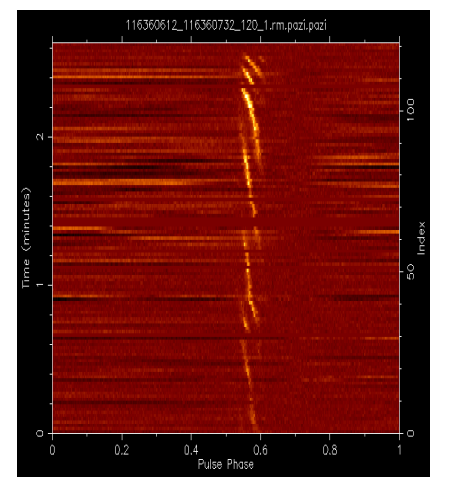
(c) Integrated profile (before cleaning)



(d) Integrated profile (after cleaning)



(e) RFI obstructing driftbands



(f) Clear driftbands post-cleaning

Figure 3.1: Comparison of uncleaned (left column) and cleaned (right column) data: Frequency-phase plots, integrated profiles, and driftband clarity across 120 pulses.

3.1.2 Averaged Polarization Profile

Using the RFI cleaned data, we converted the polarisation coherence parameters into the standard Stokes parameters (I, Q, U, V). For the 41st and the 47th cycle data, a multi-step cleaning and transformation procedure was applied to ensure the quality and consistency of the observational dataset. The data contained polarization information in terms of the coherence parameters: AA, BB, CR, and CI, where AA and BB are the auto-correlation products of the input channels A and B, and CR and CI are the real and imaginary parts of the cross-correlation $A \times B$, with A representing the left circular feed and B the right circular feed.

Initially, corrupted subintegrations were identified using the metadata flag subint=X chan=0 zapped, which indicates interference or unusable data for the corresponding pulse number. These entries were extracted using regular expressions and subsequently replaced with 512 synthetic rows—each corresponding to a phase bin from 0 to 511—with all coherence parameters set to zero. This ensured uniform structure across all pulses.

The modified data were parsed using pandas into a tabular format, with numerical conversion applied to ensure consistency. From the cleaned dataset, the Stokes parameters were computed as follows:

$$I = AA + BB$$
, $Q = 2CR$, $U = -2CI$, $V = AA - BB$

These transformations enabled the recovery of total intensity, linear polarization components, and circular polarization from the recorded voltage correlations. The resulting data were saved in a standardised format for use in subsequent polarimetric and statistical analyses.

The data are reshaped into pulse matrices, average intensity profiles are computed, and the linearly polarised intensity $(\sqrt{Q^2 + U^2})$ is calculated. We then plot the total intensity (I), linearly polarized intensity and circularly polarised intensity (V) as shown in Figure 3.2 using black, red, and blue colors, respectively. Figure 3.3 shows the polarization profile of the 47th cycle data, indicating that the circular component exceeds the linear components in the pulse window. This occurs due to polarization leakage stemming from calibration inaccuracies in the instrument.

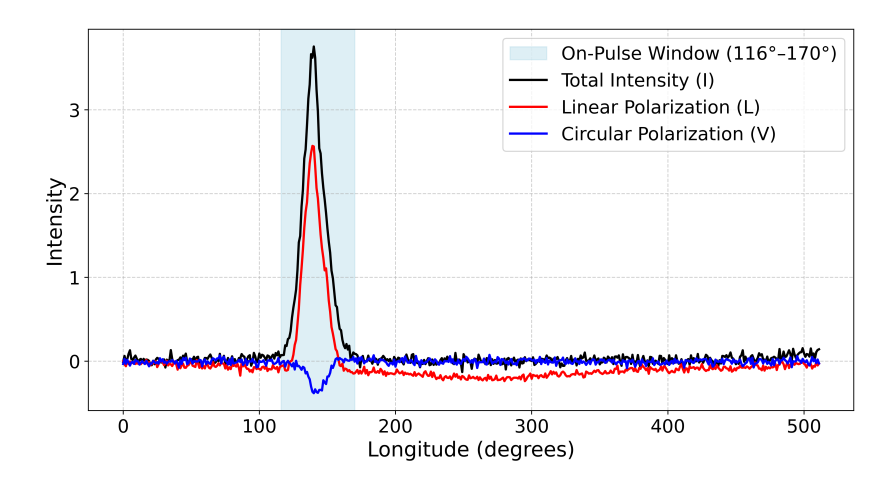


Figure 3.2: Observation cycle-37: Average Profile in total (black), linear (red), and circular polarisation (blue) vs longitude.

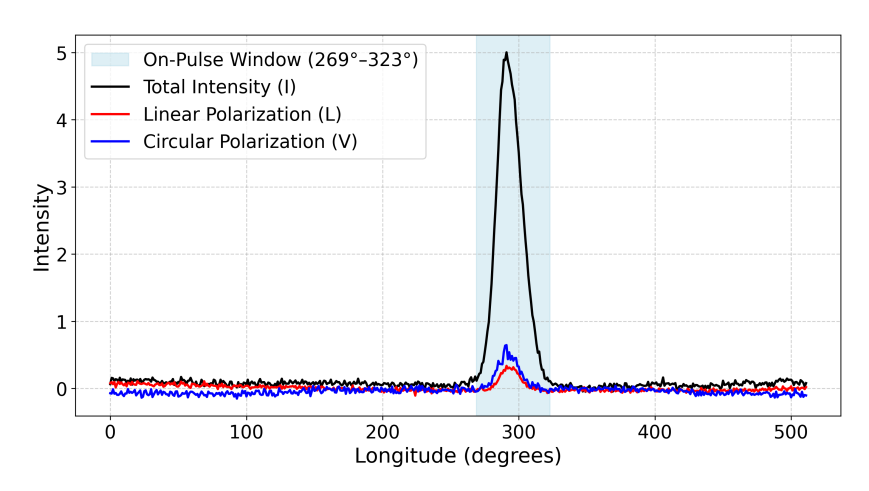


Figure 3.3: Observation cycle 47: Average Profile in total (black), linear (red), and circular polarization (blue) vs longitude.

We also computed the PA angle sweep and θ , the circular contribution angle of the full profile, displayed in Figure 3.4. Observe how the S-curve is varying smoothly and θ (circular polarisation contribution angle) is high at the central longitude of the overall profile.

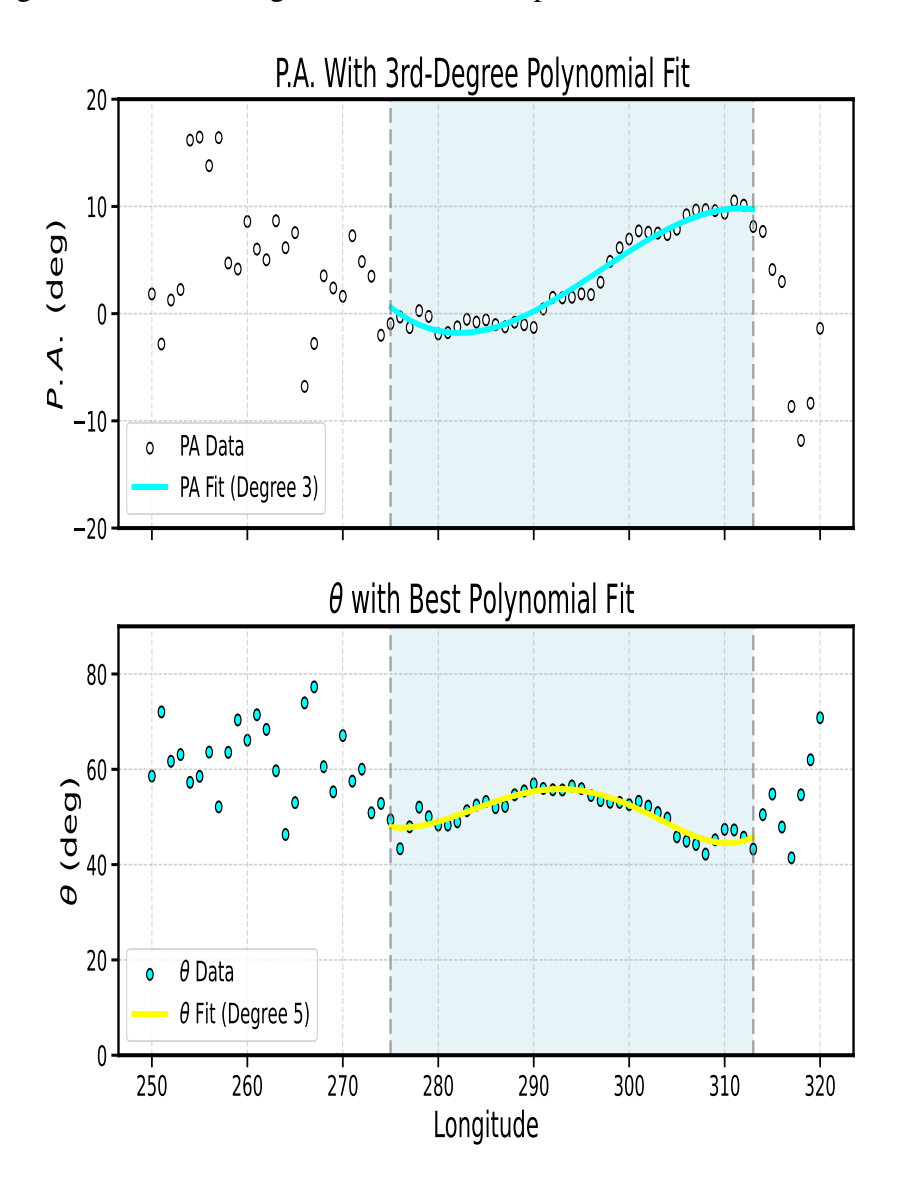


Figure 3.4: cycle-47 Observation: Top: The longitude averaged position angle (PA) curve of linear polarisation across pulse longitude. The PA is calculated using the relation PA = $\frac{1}{2} \tan^{-1} \left(\frac{U}{Q} \right)$, which describes the orientation of the linear polarisation vector. Bottom: The circular contribution angle $\theta = \tan^{-1} \left(\frac{V}{L} \right)$, where $L = \sqrt{Q^2 + U^2}$, characterizes the relative dominance of circular to linear polarisation. Higher values of θ indicate stronger circular polarisation contributions.

3.1.3 Longitude-Resolved Fluctuation Spectrum (LRFS)

The Longitude-Resolved Fluctuation Spectrum (LRFS) offers insight into periodic intensity variations (Stokes I) as a function of pulse longitude. It is computed via a one-dimensional discrete Fourier transform (DFT) across successive pulses for each longitude bin, revealing periodicities (typically referred to as P_3). Following Edwards 2004,

$$L_{kl} = \frac{1}{N} \sum_{n=1}^{N} e^{-2\pi i n k/N} \left(I_{nl} - \langle I_l \rangle \right)$$

where

- N: Total number of pulses.
- I_{nl} : Intensity in longitude bin l for pulse n.
- $\langle I_l \rangle$: Mean intensity at longitude bin l.
- *k*: Frequency index in the Fourier domain.
- L_{kl} : Fourier component at frequency k and longitude bin l.

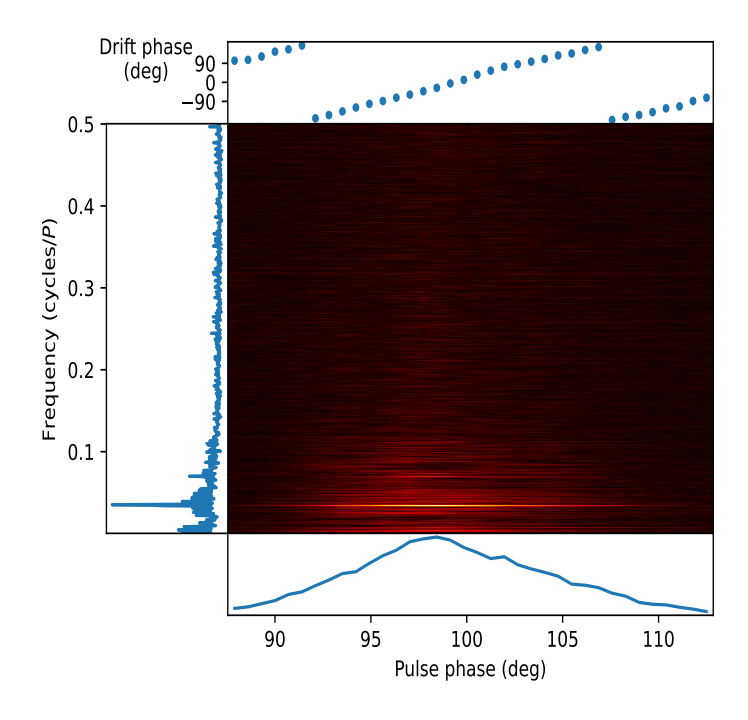


Figure 3.5: cycle-47 Observation: LRFS. Bottom: Integrated pulse profile. Longitude-Resolved Fluctuation Spectrum (LRFS) showing a peak near 0.04 cycles per rotation, indicating an average subpulse repetition period (P_3) of approximately 25 pulses.

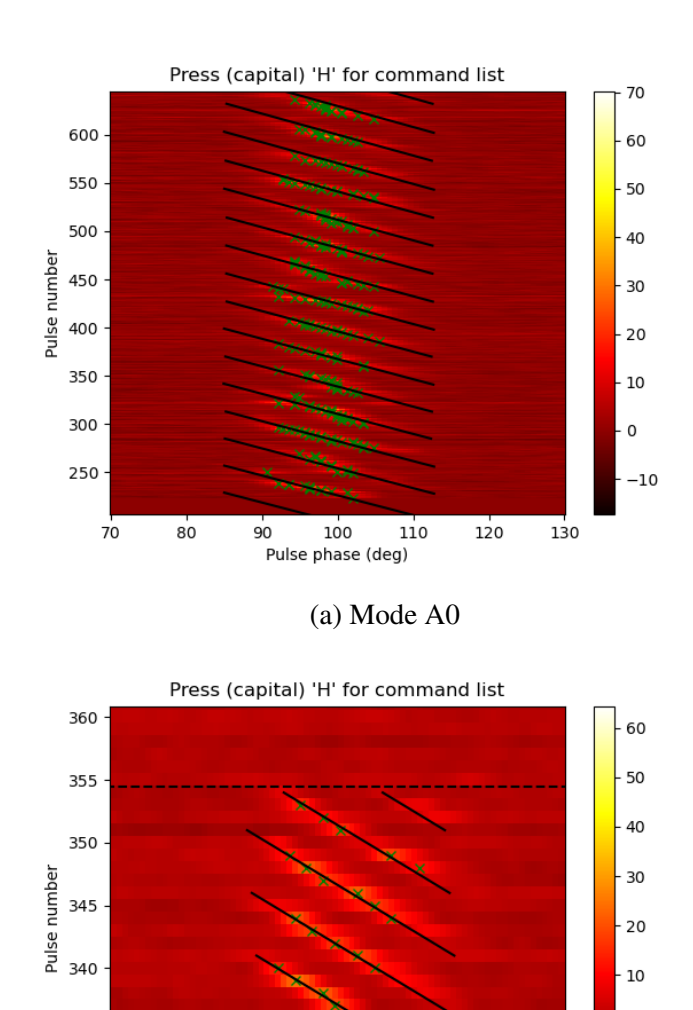
The LRFS, as shown in Figure 3.5, gives us the average P_3 value at various longitudes. From the figure, we can infer that the frequency is approximately 0.04 cycles per pulsar rotation period. This implies that we expect subpulse phase repetitions for every 25 pulse cycles on average. While LRFS provides useful insights into the periodic variations in pulse numbers (P_3) , it restricts our understanding of how these variations influence periodicity when different modes exist within a drift band. Consequently, we cannot fully grasp how evolutionary drifting and other features contribute to the overall LRFS.

3.1.4 Drift Band Fitting

We performed a visual inspection of drift transition features using software developed by S. McSweeney. These data were previously analysed by Janagal et al. 2023 to study phenomena such as evolutionary drifting, rapid mode changes, and nulling.

- We identified several interesting characteristics in pulse stacks, including various drifting modes:
 - Fast drifts
 - Slow drifts
 - Stable drifts
 - Evolutionary drifts
- Noted both broken and connected drift bands.
- Observed points of rapid mode switching.
- Marked all peak intensities in the pulse stack.
- We determined subpulse drifts based on:
 - A threshold set for individual subpulse intensities.
 - A visually established onpulse region.
- Divided pulse stacks into different modes through visual inspection.
- Assigned mode boundaries.
- Selected peak markers to fit the best lines or curves.

- Assigned drift band numbers in each mode.
- Employed quadratic fitting to capture the curvature of drift bands:
 - The figures: 3.6 and 3.7 show the fitted drift bands of different modes.



(b) Mode B

210

Pulse phase (deg)

220

230

335

330

180

190

200

0

-10

Figure 3.6: Modes A0 and B. The black lines illustrate the quadratic fits, while the green crosses denote the subpulse peaks. The software utilizes these green crosses to apply linear and quadratic models, effectively representing the drift bands.

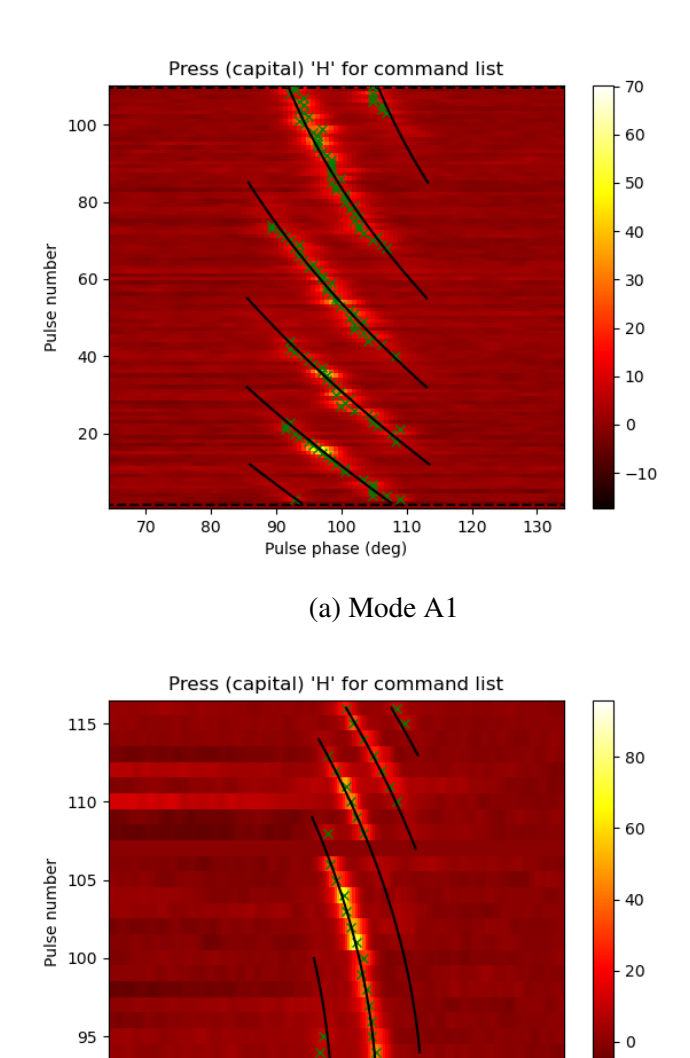


Figure 3.7: Modes A1 and A2. The black curves illustrate the quadratic fits, while the green crosses denote the subpulse peaks. The software utilizes these green crosses to apply linear and quadratic models, effectively representing the drift bands.

(b) Mode A2

.80 200 220 Pulse phase (deg)

240

260

90

140

160

180

An analysis of the full-intensity mode was presented by Janagal et al. (2023), which identified four distinct categories of drift modes for this pulsar. These modes are classified based on their P_3 and P_2 values. Stable modes (A0 and B) exhibit a constant P_3 value, while evolutionary modes have two subtypes (A1 and A2): slow-to-fast and fast-to-slow.

In the slow-to-fast mode, the peak shifts in phase slowly at earlier pulses and accelerates at later pulses, creating a curved shape that becomes more horizontal as the pulse number increases. In contrast, the fast-to-slow mode begins with rapid drifting that gradually slows down over time. For evolutionary drifting, we utilize quadratic and exponential fitting, while for stable drifting, we apply linear fitting.

We are using the same nomenclature as Janagal et al. (2023) in our analysis, which includes A0, A1, A2, and B. Utilising this system, we fitted the data and identified the occurrences of the four modes in our sample. The figures 3.8, 3.9 show that for the A0 drift mode, the drift rate peaks at -0.5(deg/P), while for the B drift mode, it peaks at -1.5 (deg/P). The spread of the curve for A0 and B modes is narrower and more pointed compared to the A1 and A2 modes. This is because A0 and B modes are stable drift modes, leading to more consistent drift rates. This allowed us to derive P_3 as a function of pulse number for the different mode occurrences. This variation of P_3 is displayed in Figure 3.10, which demonstrates the change in P_3 from slow to fast and fast to slow, especially for the evolutionary drift modes.

Drift Rate Histograms by Mode Mode A0 Mode A1 Drift Rate (deg/P) Mode A2 Mode B Mode B Mode B Mode B Mode B Mode B

Figure 3.8: **Drift Rate Distributions by Mode:** Histograms of subpulse drift rates for different drift modes.

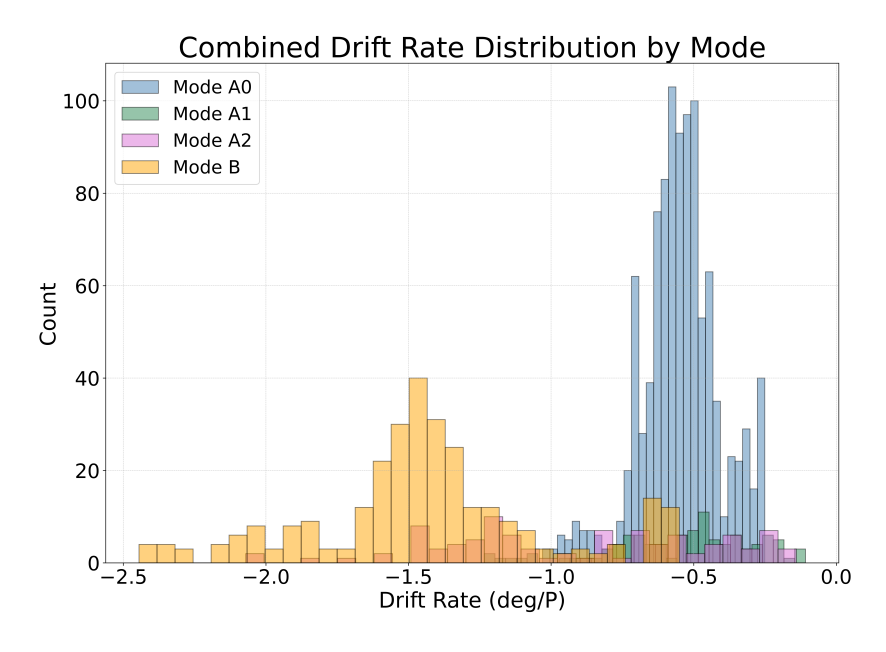


Figure 3.9: Histogram of drift rate distribution: X-axis for drift rate, Y-axis for occurrences.

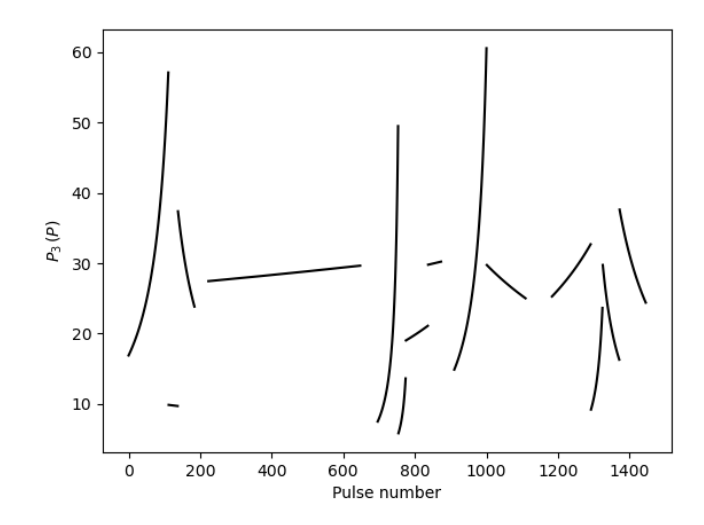


Figure 3.10: P_3 as a function of pulse number. Constant P_3 value indicates stable drift modes A0 and B; increasing P_3 indicates A1 mode; and decreasing P_3 indicates A2 modes in the pulse numbers.

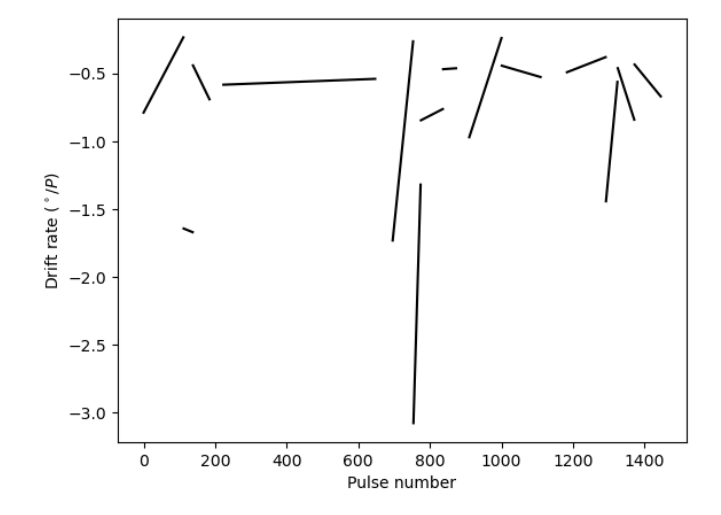


Figure 3.11: Drift rate as a function of pulse number. A constant drift rate indicates stable drift modes, while increasing and decreasing drift rates represent slow-to-fast and fast-to-slow drift modes, respectively. The negative sign indicates the peak is shifting earlier in phase compared to the last period.

3.1.5 Interesting Drifting Features

Subpulse drifting in pulsars is categorized into different modes based on the evolution of the drift rate across pulse sequences. Mode A0 features a stable, nearly constant drift rate of approximately $-0.6^{\circ}/P_1$. Mode A1 shows a gradual evolution from fast to slow drift rates. Mode A2 begins with a slow drift rate and evolves to a faster one. Mode B is characterized by a faster drift, with a drift rate of approximately $-1.5^{\circ}/P_1$, typically producing more closely spaced driftbands than in the A0 modes.

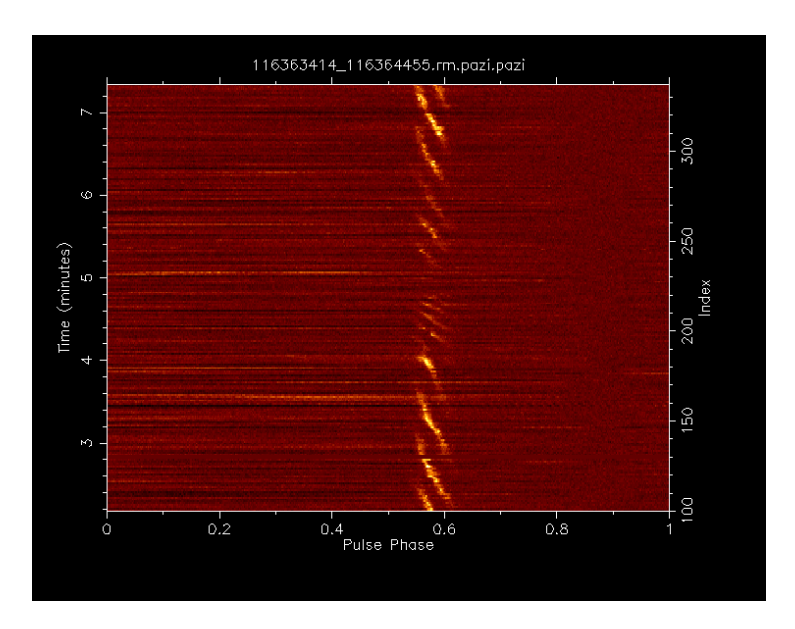
Analyzing the long dataset has revealed several intriguing features that contribute to our understanding of the pulsar's behaviour over time. A particularly notable observation is the transition of the drift bands from higher P_3 values to lower P_3 values and then back to higher P_3 . This transition is indicative of a shift in the pulsar's mode, specifically from the A0 mode to an evolutionary mode and back. This shift is visually represented in Figure 3.12a, where the sequence of modes follows the pattern: $A0 \rightarrow A2 \rightarrow Null \rightarrow A1 \rightarrow A0$.

In Figure 3.12b the behaviour of the drift bands in these transitions appears smooth and continuous, with the lower half of the bands drifting from slow to fast, while the upper half shifts from fast to slow. The smoothness of the transitions could point to underlying physical processes that act rapidly but in a controlled manner.

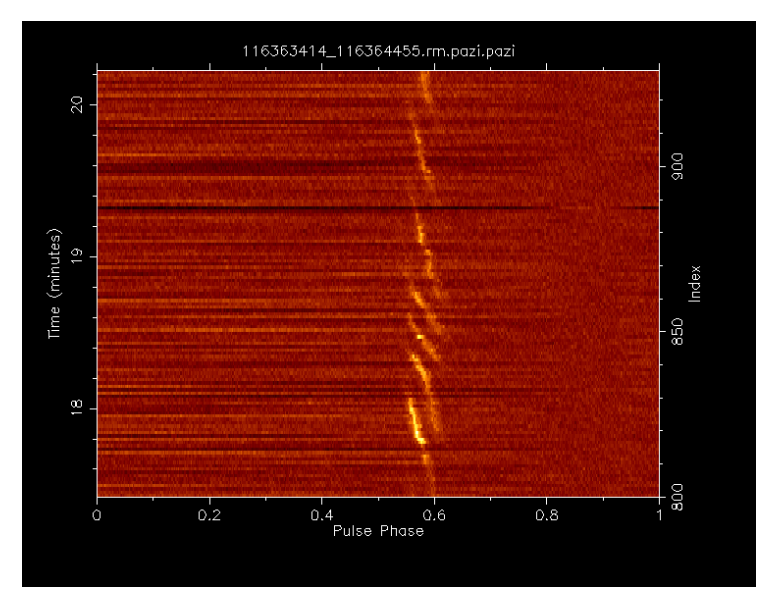
Further analysis has also revealed sudden, rapid mode transitions. These transitions, illustrated in Figure 3.13b, involve sudden shifts between different drift rates, suggesting that the pulsar's emission mechanism maybe undergoing abrupt changes.

Finally, the observation of nulls, particularly in polarisation, as shown in Figure 3.13a, offers another useful dimension to the data. During these null intervals, the pulsar emission vanishes or becomes highly attenuated, which could be indicative of a temporary cessation of coherent emission or a shift in the emission geometry. By investigating these nulls under polarisation lenses, we can explore whether new phenomena emerge

during these intervals. It is possible that these nulls represent a transient phenomenon, such as a brief reconfiguration of the pulsar's magnetic field, or a change in the plasma density around the pulsar.

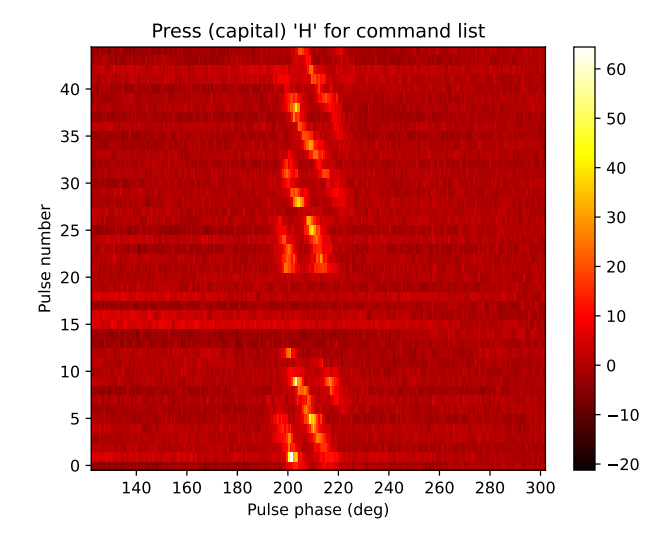


(a) Drift bands transition from broad to slim to broad, indicating A0 \rightarrow evolutionary mode and back. Sequence: A0 \rightarrow A2 \rightarrow Null \rightarrow A1 \rightarrow A0.

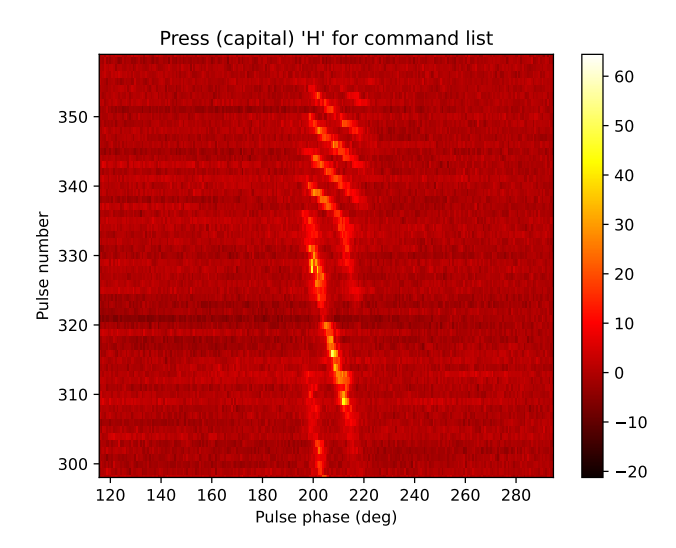


(b) Switch between modes A and B. Lower half drifts slow \rightarrow fast, upper half fast \rightarrow slow.

Figure 3.12: Illustration of gradual drift mode transitions and switching between different drift states.



(a) The pulse stack showing a null between two B modes.



(b) Switch between modes A0 and B. The lower half shows broader drift bands, while the upper half shows slimmer drift bands.

Figure 3.13: Illustration of Nulling, rapid drift mode transitions and switching between different drift states.

3.1.6 Polarimetric view of the four subpulse drifting modes

Figures 3.14, 3.15 and 3.16, 3.17 show the Stokes parameters and corresponding derived polarisation properties after applying a Gaussian smoothing ($\sigma = 1.5$) before imposing an intensity threshold on the total intensity I. This thresholding suppresses low signal-to-noise regions, ensuring that the derived quantities—ellipticity angle, position angle, and fractional linear and circular polarisation—are representative of mean-

ingful emission features. As a result, these visualisations emphasise the coherent structure in the pulsar's polarisation state and enhance the clarity of weak drift patterns by excluding noisy background regions. Note that the fractional linear polarization and fractional circular polarization drifts show very little variation in the full pulse stack.(see figure 3.15, 3.17)

Figures 3.18, 3.19, 3.20, and 3.21 present the Stokes parameters (I, Q, U, and V) for the drift modes A0, A1, A2, and B, respectively. In each figure, the X-axis denotes the pulse longitude, while the Y-axis corresponds to the pulse number. The color bar indicates the magnitude of each respective Stokes parameter, enabling a visual assessment of polarization properties as a function of pulse phase and time.

A noteworthy feature across these visualizations is the presence of periodic drift bands in the linear polarization components Q and U(see figure 3.18, 3.19, 3.20, 3.21). These drift bands exhibit alternating positive and negative values, reflecting transitions among vertical, horizontal, and slanted linear polarization states along pulse longitude. This behaviour is consistent across all modes, suggesting a coherent and structured evolution of the linear polarization vector within each mode.

The circular polarization component V reveals particularly interesting behavior. In modes A1, A2, and B, the V component displays clearly defined drift bands with periodic structures, indicating the presence of systematic circular polarization modulation. Most strikingly, in the evolutionary drift modes A1 and A2, the V component occasionally switches sign—effectively reversing the handedness of circular polarization. These sign reversals are not only sharp but occur within specific longitude regions, that might suggest underlying magnetospheric processes that alter the emission geometry or propagation conditions.

Synchronous variations among Q, U, and V are apparent in all drift modes, but they are especially pronounced in the evolutionary modes A1 and A2. In these modes, the drift structures across all Stokes parameters are phase-locked, indicating a high degree of polarization coherence. Such behavior may reflect changes in the emission altitude, beam shape, or mode switching dynamics.

Overall, our plots emphasize the complex and mode-dependent polarization behavior of the pulsar, with distinct signatures in both linear and circular components that evolve systematically with drift mode.

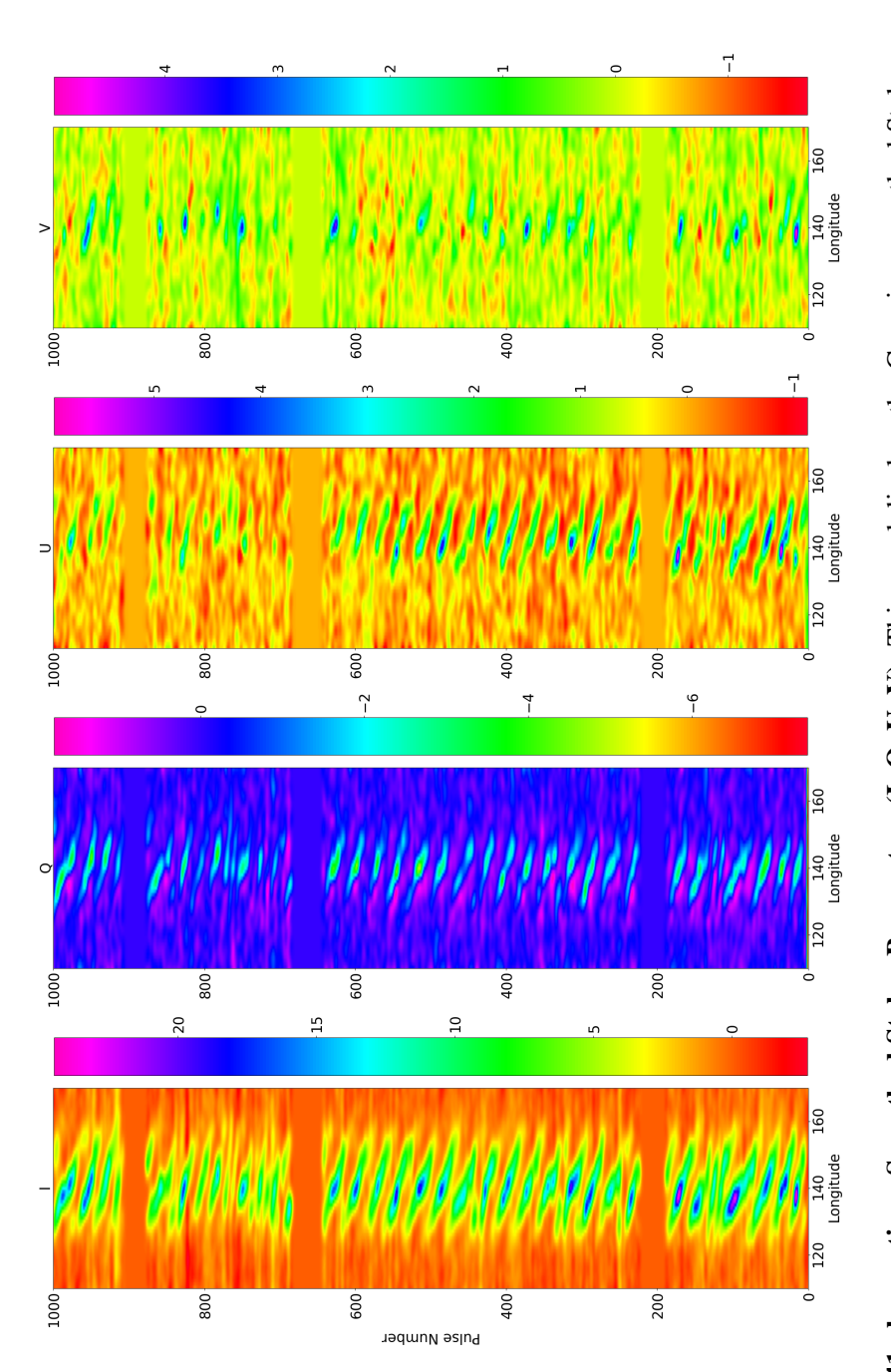
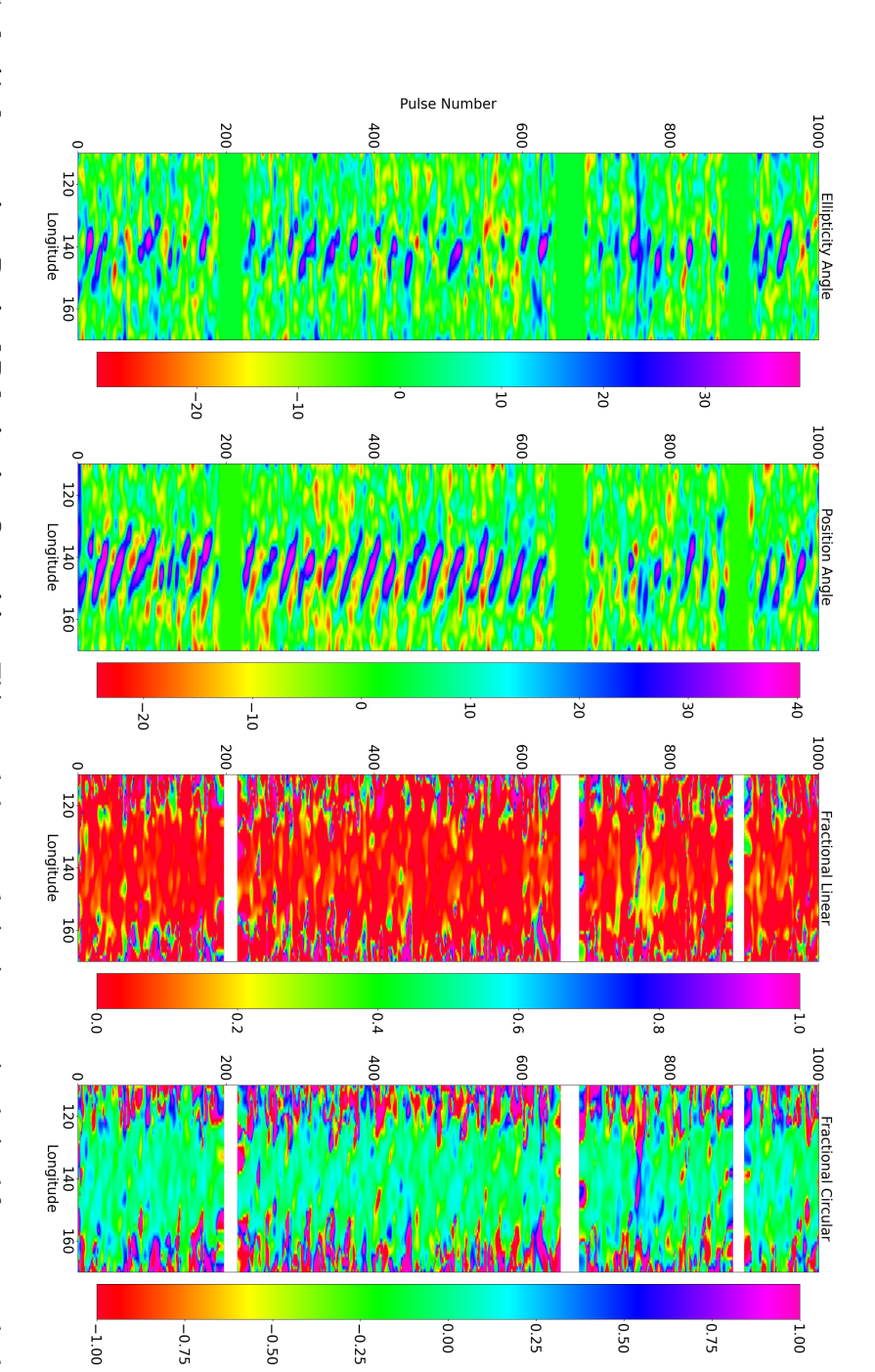


Figure 3.14: Cycle-41 observation: Smoothed Stokes Parameters (I, Q, U, V): This panel displays the Gaussian-smoothed Stokes parameters across pulse number and pulse longitude within the window 110-170. Each subpanel corresponds to one of the Stokes components, highlighting the intensity and polarization structure of the emission. Gaussian smoothing with $\sigma = 1.5$ enhances coherent features while suppressing noise.



ellipticity angle (EA) and position angle (PA) trace the geometry of the polarization, while the fractional linear (L) and fractional circular (C) polarizations quantify the strength of linear and circular components relative to total intensity. Figure 3.15: Cycle-41 observation: Derived Polarization Quantities: This panel shows polarization metrics derived from smoothed Stokes parameters. The

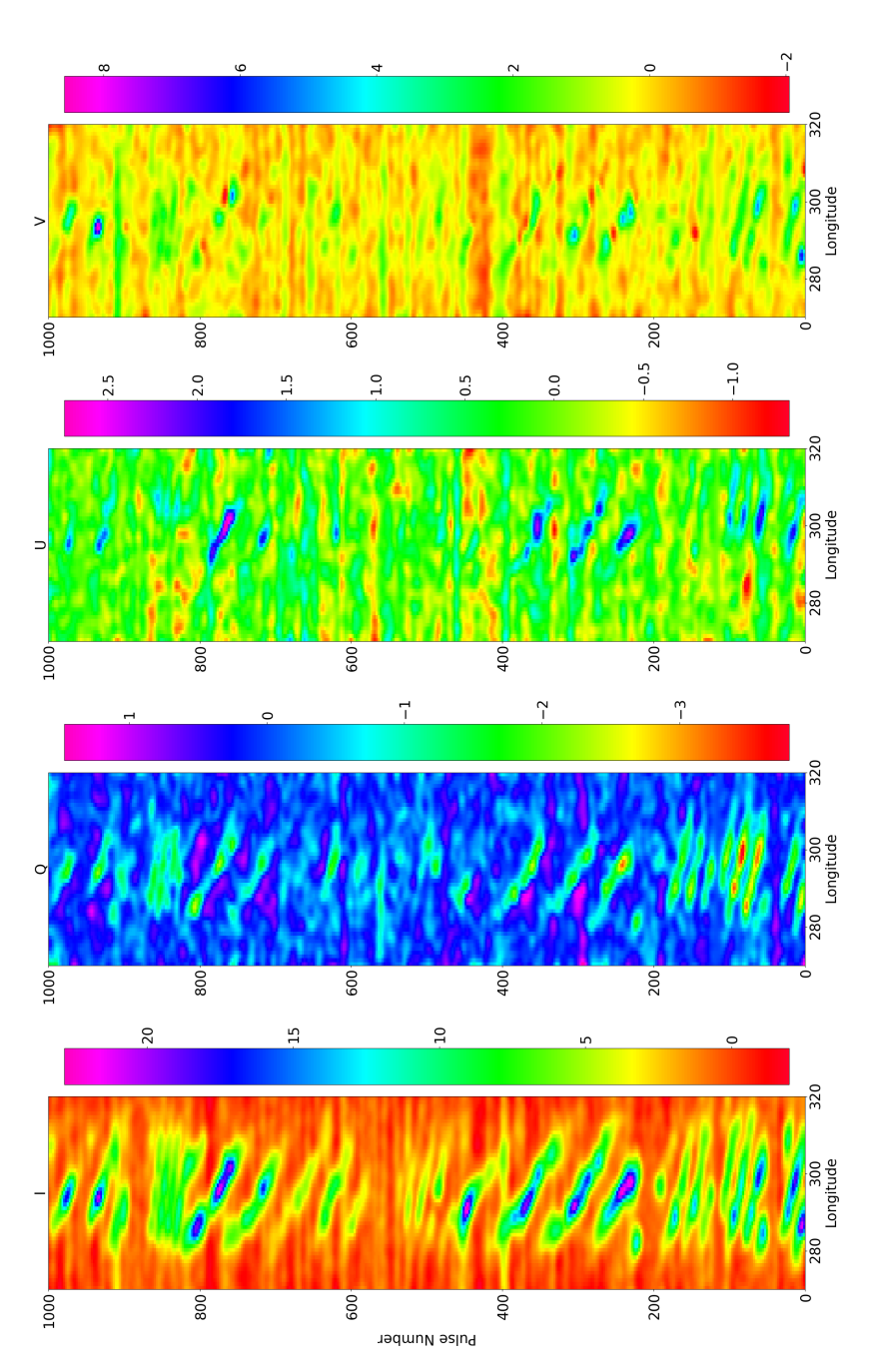
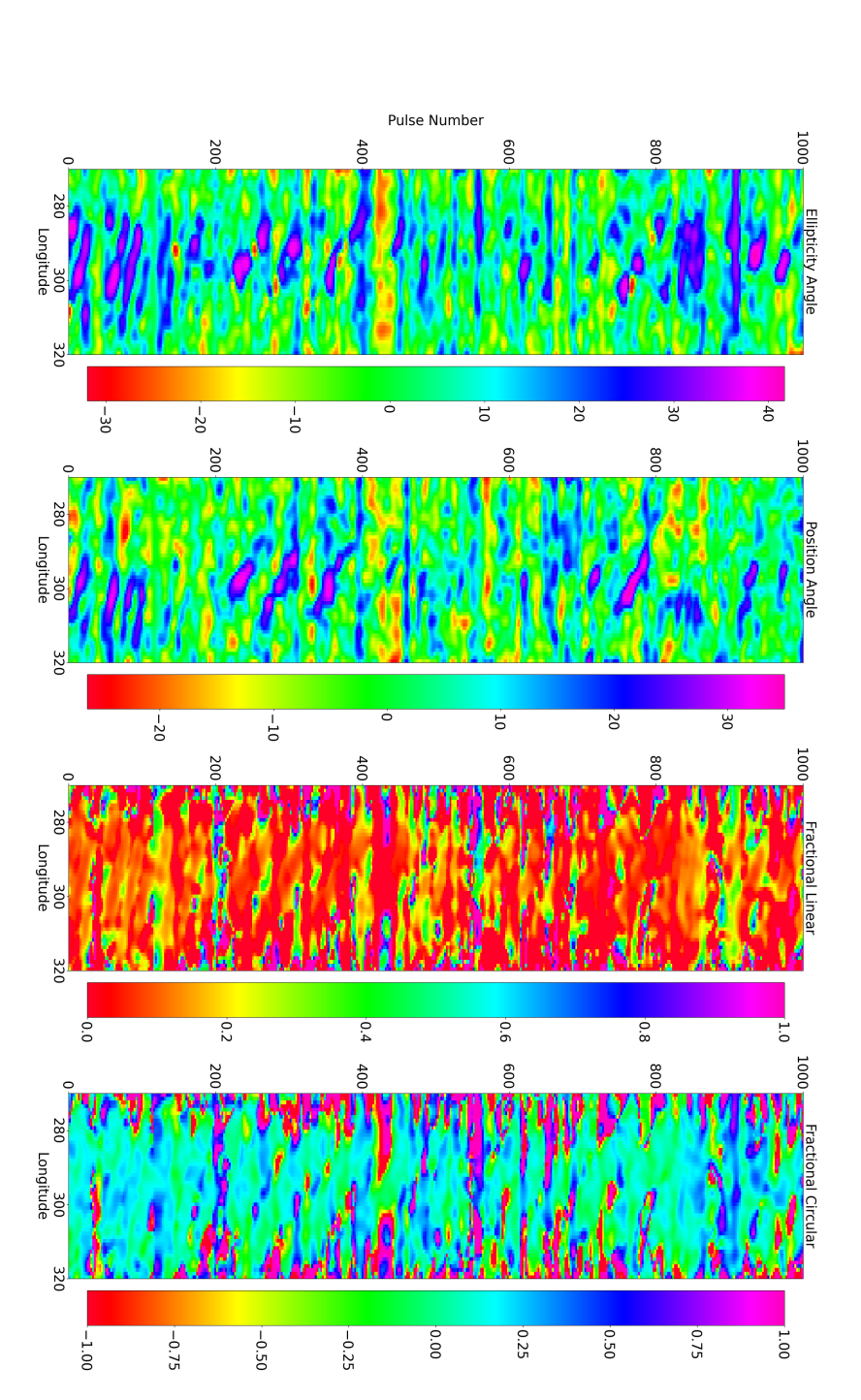


Figure 3.16: Cycle-47 observation: Smoothed Stokes Parameters (I, Q, U, V): This panel displays the Gaussian-smoothed Stokes parameters across pulse number and pulse longitude within the window 270-310. Each subpanel corresponds to one of the Stokes components, highlighting the intensity and polarization structure of the emission. Gaussian smoothing with $\sigma = 1.5$ enhances coherent features while suppressing noise.



ellipticity angle (EA) and position angle (PA) trace the geometry of the polarization, while the fractional linear (L) and fractional circular (C) polarizations quantify the strength of linear and circular components relative to total intensity. Figure 3.17: Cycle-47 observation: Derived Polarization Quantities: This panel shows polarization metrics derived from smoothed Stokes parameters. The

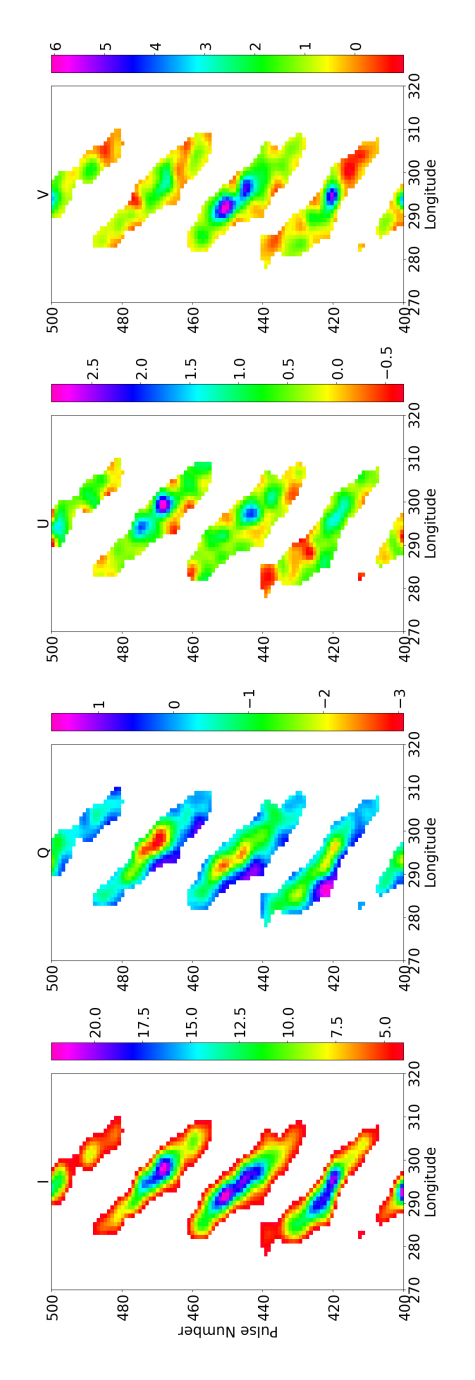
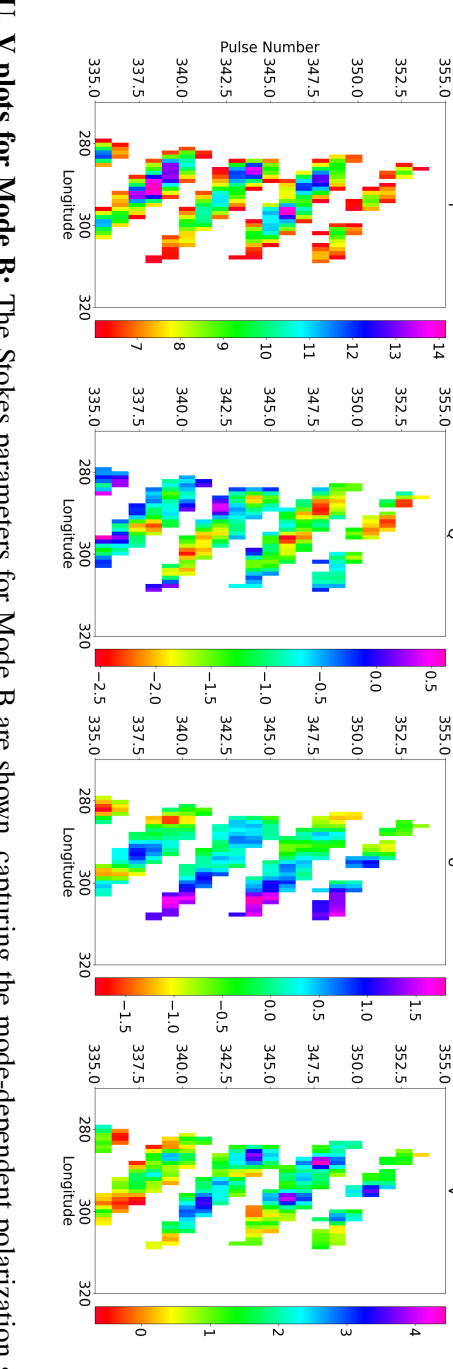


Figure 3.18: I, Q, U, V plots for Mode A0: This figure shows the Stokes parameters for Mode A0. The total intensity (I), linear polarization components (Q and U), and circular polarization (V) are plotted across pulse phase to analyze polarization behavior in this mode.



longitude. The variations in Q, U, and V highlight changes in polarization geometry. Figure 3.19: I, Q, U, V plots for Mode B: The Stokes parameters for Mode B are shown, capturing the mode-dependent polarization structure across pulse

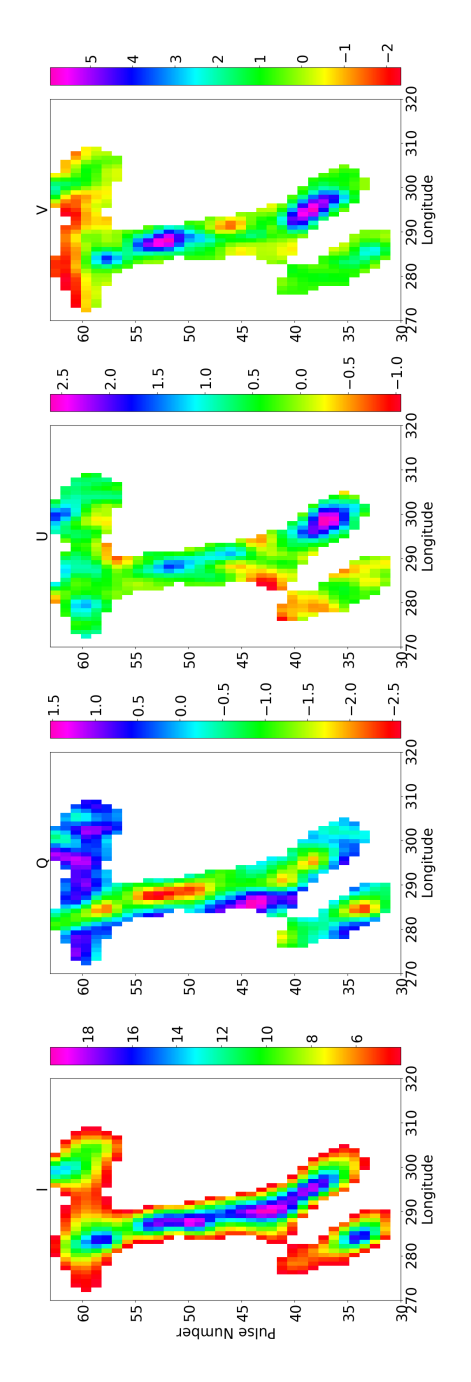


Figure 3.20: I, Q, U, V plots for Mode A1: Polarization profiles for Mode A1, illustrating the behavior of intensity and polarization components across the pulse. These help identify distinguishing polarization patterns for this mode.

Pulse Number 110 115 100 290 300 Longitude 310 20 100 25 30 35 105 290 300 Longitude 310 Ĺ 100 105 110 270 280 290 300 Longitude 310 290 300 Longitude 310 320

of this drift mode. Figure 3.21: I, Q, U, V plots for Mode A2: This figure presents the Stokes profiles for Mode A2, showing the temporal evolution and polarization characteristics

Position Angle (PA)

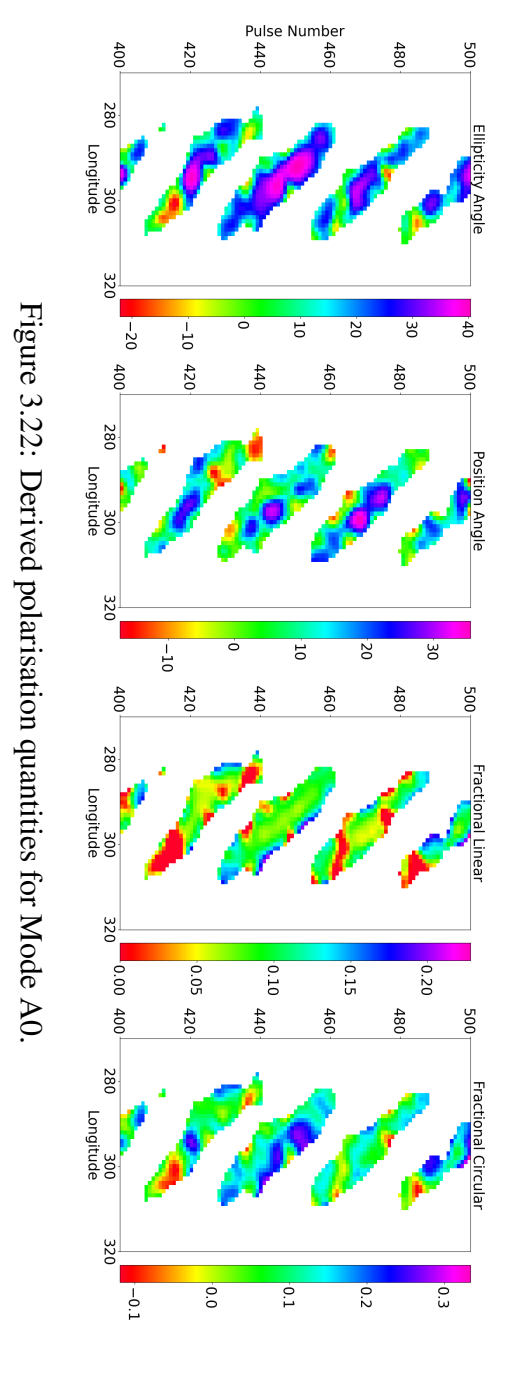
The position angle plots clearly show a transition from positive to negative values for all the modes, as illustrated in Figures 3.22, 3.23,3.24 and 3.25. The variation of the position angle along the phase can be effectively explained by the Rotating Vector Model (RVM). The drift synchronous behaviour is highly noticeable in all the modes. We can note the 0 to negative values in the position angle values in the left half of the pulse window (3.24,3.25). However, the synchronous drift transition in the position angle presents a challenge for the RVM model.

Ellipticity Angle

The ellipticity angle plots in Figures 3.22, 3.23 3.24 and 3.25 illustrate how the ellipticity angle varies across four distinct drift modes. Notably, we observe sign changes related to variations in both longitude and pulse number. As shown in these figures, the ellipticity angle displays a pattern of increase and decrease, along the drift bands. This indicates a transition between circular and linear behaviour. This periodic behavior is showing at least twice in every mode. This pattern of increase and decrease is most prominently seen in evolutionary drift modes A1 and A2 as shown in the figures 3.24, 3.25.

Fractional Linear and Fractional Circular Polarisation

Using the definitions of linear and circular polarization, we measured the fractional linear and fractional circular polarizations, as shown in figures 3.22, 3.23,3.24 and 3.25. The observations of linear polarization display a drift-synchronous pattern, with high linear polarization observed at the central longitudes for all modes. The circular polarization plots reveal a periodic behaviour for the A2 (3.24) and A1 (3.25) modes in the on-pulse region, indicating changes in the circularity in the drift.



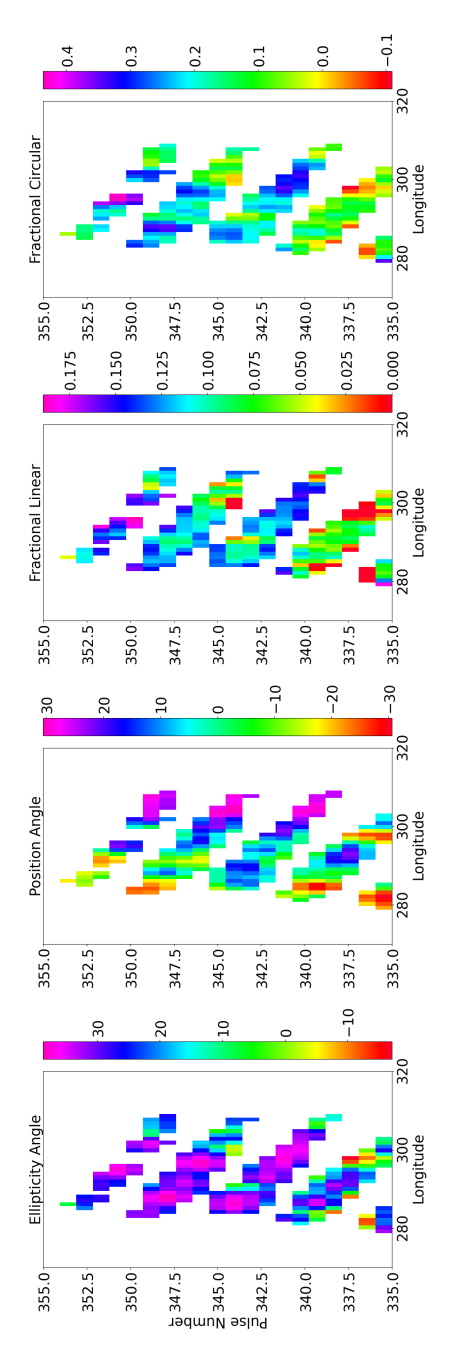
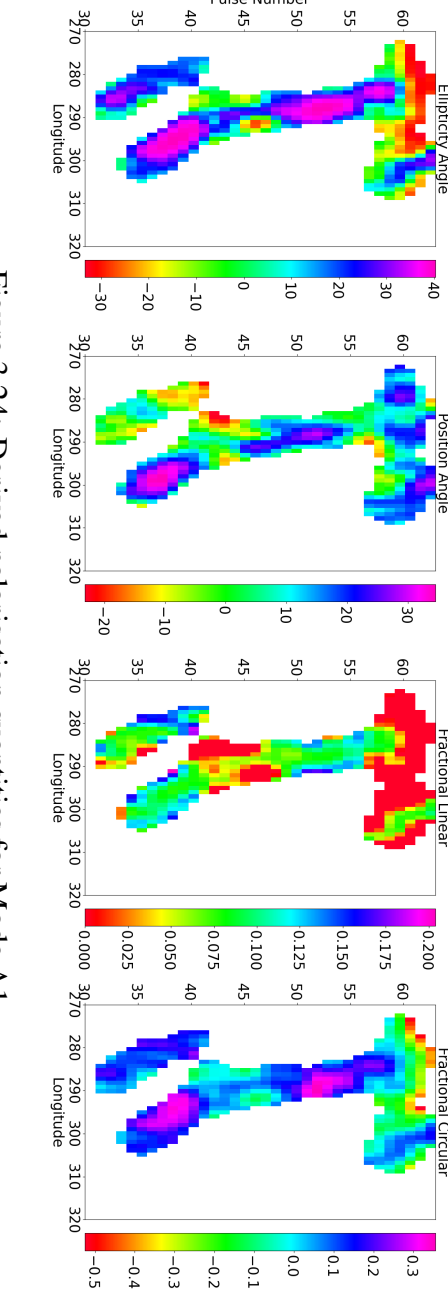


Figure 3.23: Derived polarisation quantities for Mode B.



Pulse Number

Figure 3.24: Derived polarisation quantities for Mode A1.

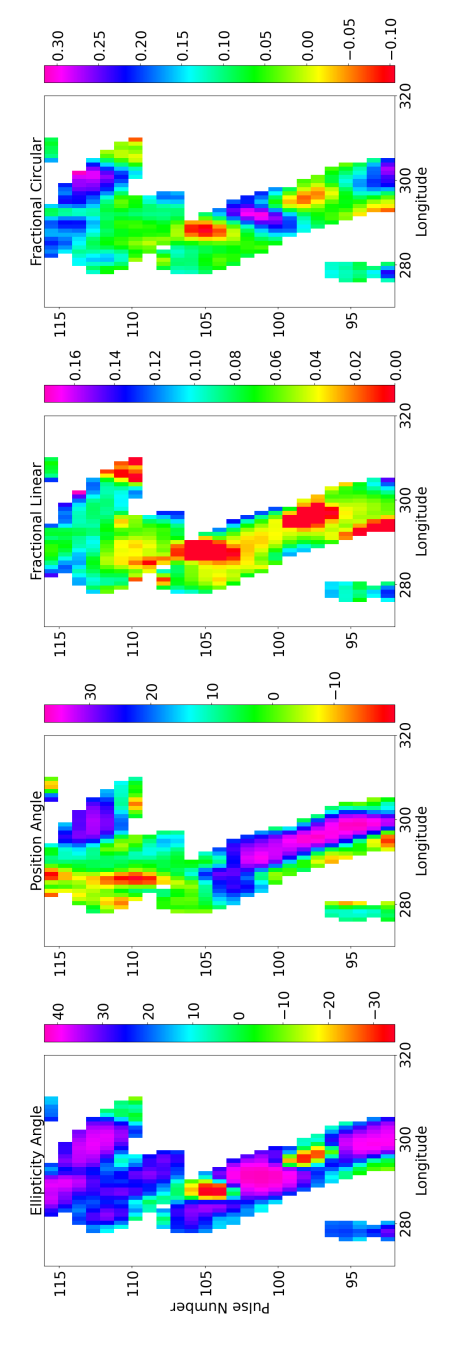


Figure 3.25: Derived polarisation quantities for Mode A2.

3.1.7 Stokes Representation of interesting features

Mode transitions—both gradual shifts toward stable states and abrupt switches between modes—are crucial for understanding the full dynamical range of pulsar behaviour. These transitions allow for a detailed, comparative analysis between different emission modes. Observing how the polarization properties evolve during these transitions helps to distinguish structural features that are intrinsic to a mode from those that result from changes in the pulsar magnetosphere. As discussed in earlier sections, both types of transitions contribute to our understanding of the interplay between pulsar emission mechanisms and magnetospheric conditions.

Our observations show that the Stokes Q, U, and V components generally follow the drift band patterns seen in Stokes I. This alignment suggests that the polarization properties are tightly coupled to the subpulse modulation and drifting behavior. Notably, the nulls observed between drift bands in Figure 3.28 appear consistently across all four Stokes parameters. These gaps imply that the "memory" of the emission pattern is preserved even during nulling episodes, supporting the idea of an underlying stable emission geometry that momentarily ceases and then resumes in phase.

In the figure 3.26 the Q, in particular, shows strong negative values at central pulse longitudes. This is interpreted as evidence for a vertically oriented electric field at those regions. Additionally, we observe that the Q, U, and V parameters tend to show breaks or discontinuities in regions where transitions between drift modes occur. These disruptions likely reflect rapid changes in the magnetospheric configuration and can serve as markers of instability or reorganization in the emission process.

In Figure 3.27, we find that the highest circular polarization (Stokes V) occurs near the central pulse longitudes during a gradual mode transition. This central peak in V is accompanied by a characteristic slope in the Stokes U component: negative values are seen on the leading edge of the pulse window, transitioning to positive values on the trailing edge. This behavior suggests a longitudinal gradient in polarization angle, consistent with a negative-to-positive sweep across the pulse phase.

Such transitions in U may reflect underlying changes in the magnetic field orientation or the geometry of the emission region during mode switching.

Circular polarization angle switches are not prominently noted in mode B, unlike in higher P_3 bands such as A0, as shown in the figure 3.29.

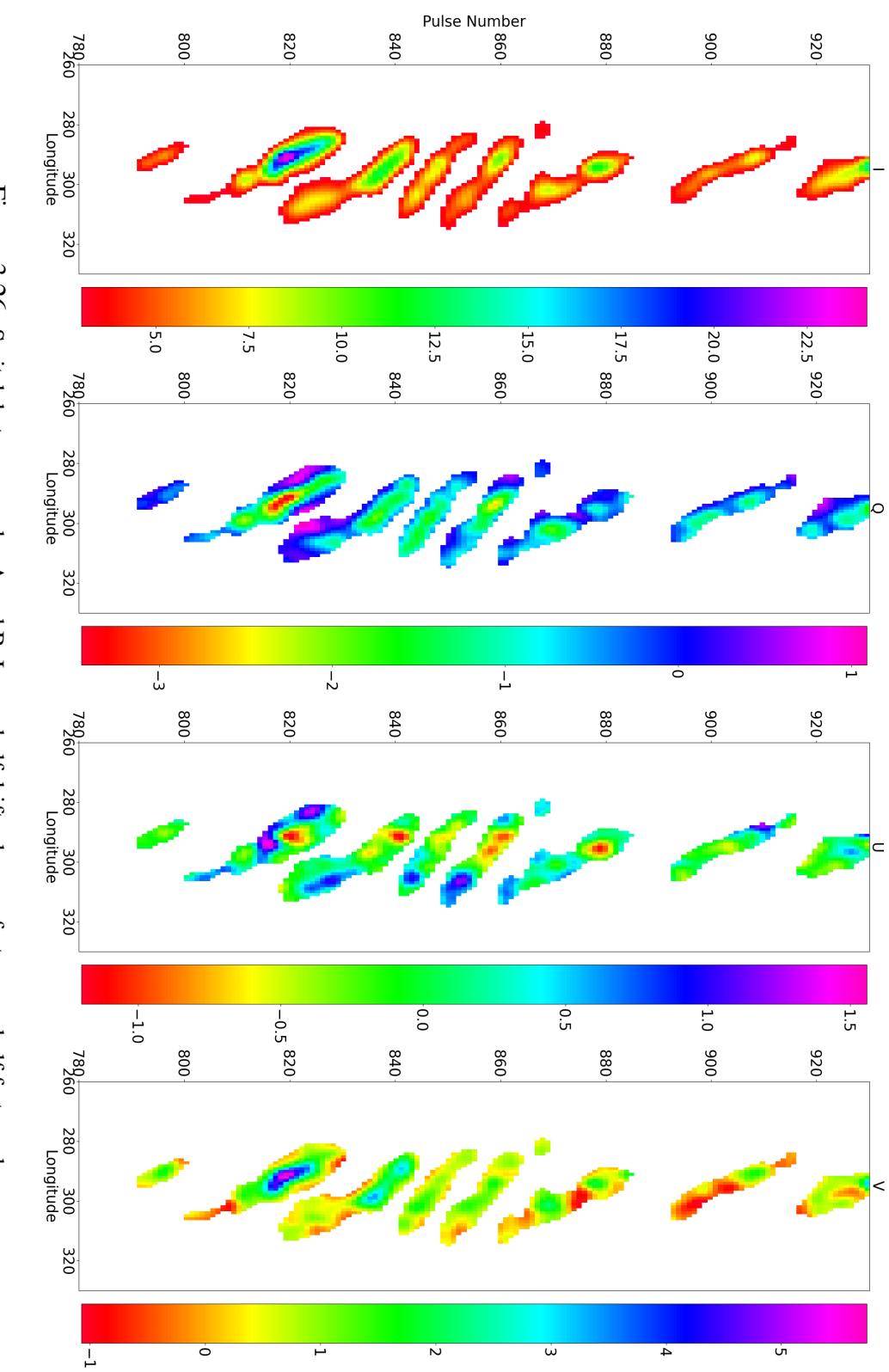


Figure 3.26: Switch between modes A and B. Lower half drifts slow \rightarrow fast, upper half fast \rightarrow slow.

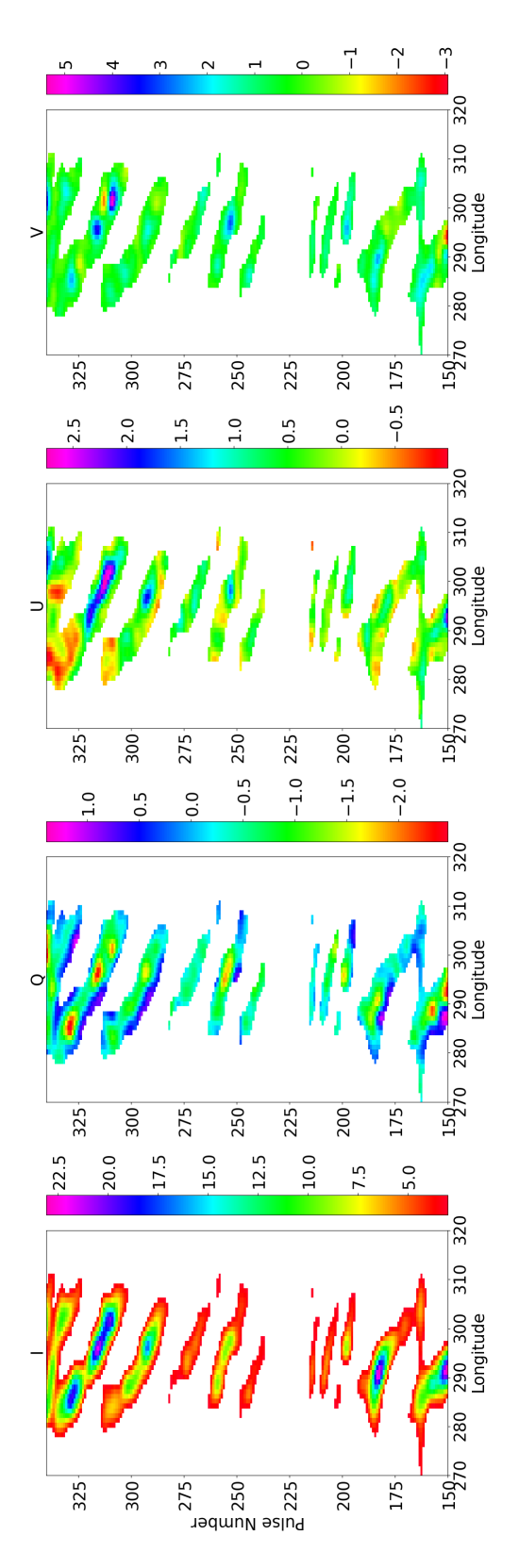


Figure 3.27: Gradual drift mode transitions and switching between different drift states in Stokes representation. $A0 \rightarrow A2 \rightarrow Null \rightarrow A1 \rightarrow A0$.

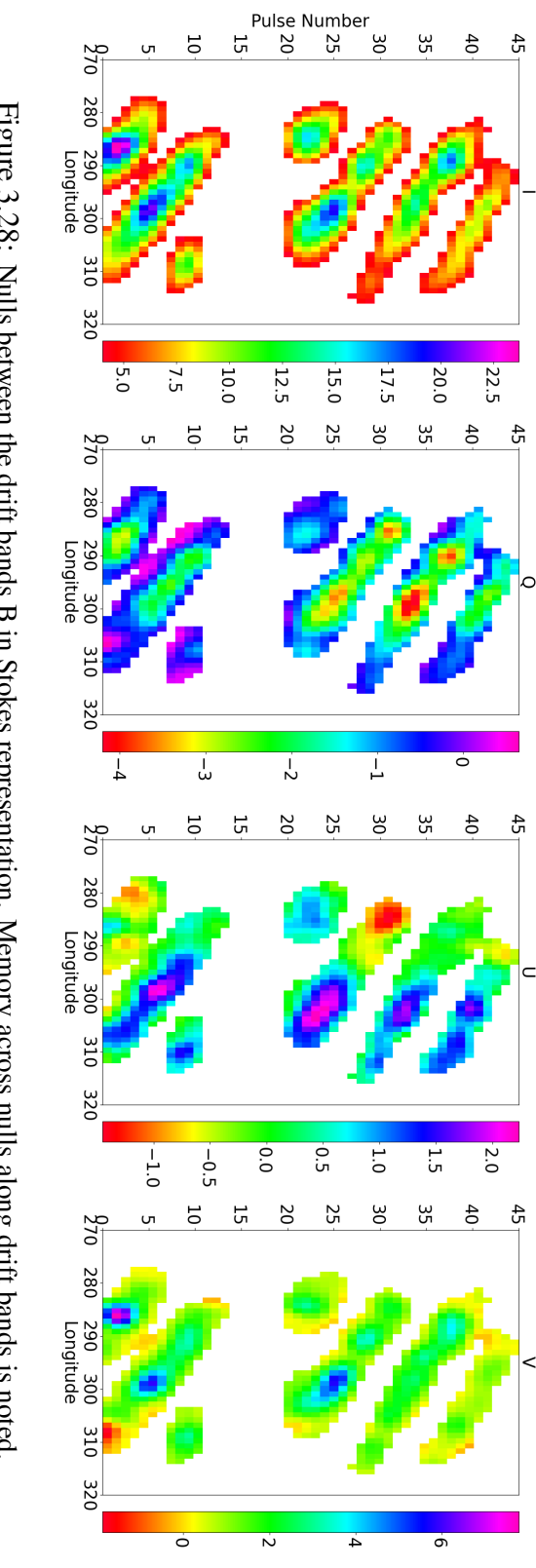


Figure 3.28: Nulls between the drift bands B in Stokes representation. Memory across nulls along drift bands is noted.

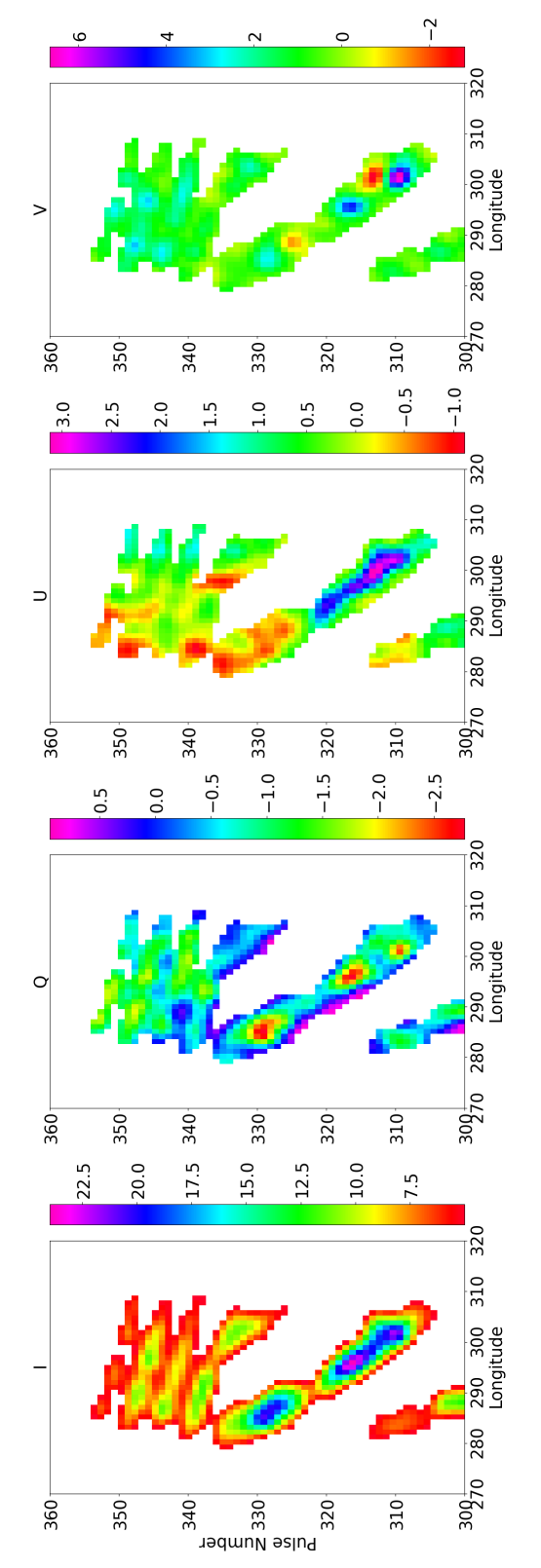
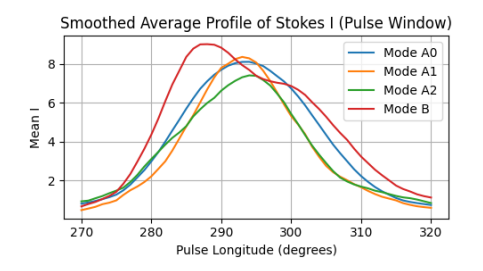
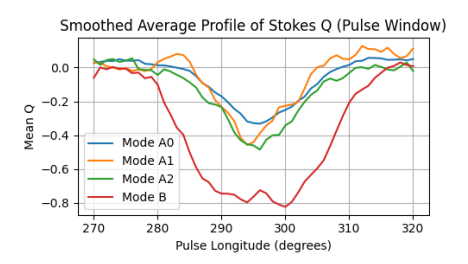


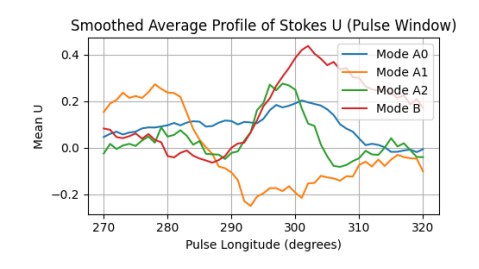
Figure 3.29: Sudden drift mode transitions between different drift states (A0 to B) in Stokes representation.

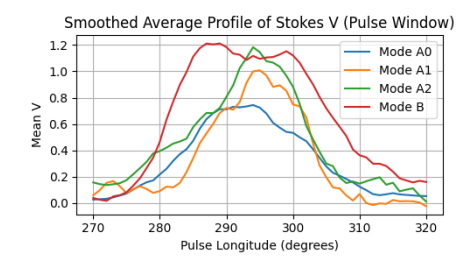




(a) Mean Stokes I over pulse longitude $(270^{\circ}-320^{\circ})$

(b) Mean Stokes Q over pulse longitude $(270^{\circ}-320^{\circ})$



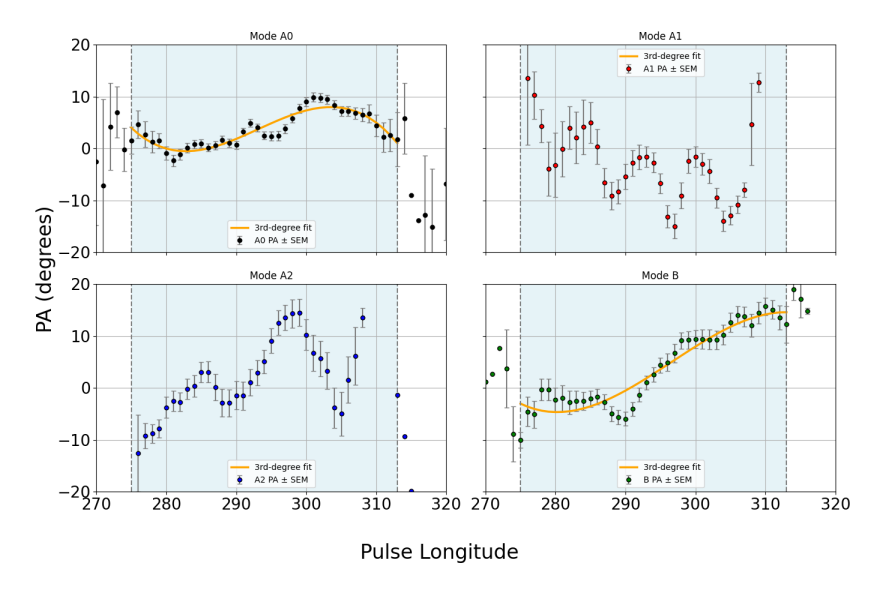


(c) Mean Stokes U over pulse longitude $(270^{\circ}-320^{\circ})$

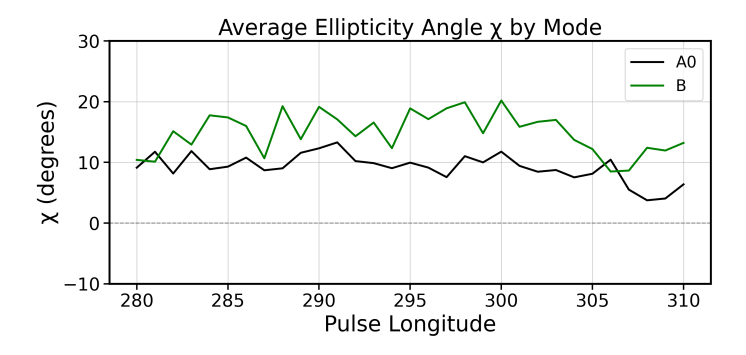
(d) Mean Stokes V over pulse longitude (270°–320°)

Figure 3.30: Mean Stokes profiles (I, Q, U, and V) across pulse longitude after pulse averaging and rolling mean smoothing within the window 270°–320°.

Notice that the pulse profile of Mode B (Figure 3.30a) appears broader compared to the other modes, suggesting a higher value of P2, which is consistent with previous findings in Janagal et al. 2023. In terms of circular polarization (Stokes V, Figure 3.30d), Modes A1 and A2 lie between the two stable extremes: A0 (lowest V) and B (highest V). For Stokes Q and U, Mode B exhibits a relatively smooth and structured pattern. Stokes Q (Figure 3.30b) indicates the most vertical polarization at the central longitude, while Stokes U (Figure 3.30c) shows a shift from -0.01 to 0.4, suggesting a transition consistent with the Rotating Vector Model (RVM). On the other hand, A0 shows the least vertical (linear) polarization at the central longitudes. The U profiles for Modes A1 and A2 display irregular and inconsistent behaviour, which could be attributed to noise, mode mixing, or artifacts introduced by the averaging and rolling mean processes.



(a) Longitude-averaged Polarization Angle (PA) profiles for drift modes A0, A1, A2, and B in the observed pulsar data. Each subplot shows the mean PA as a function of pulse longitude, computed from Gaussian-smoothed Stokes parameters and thresholded by total intensity. Error bars represent the Standard Error of the Mean (SEM) across pulses. The shaded blue region marks the longitude range used for fitting a 3rd-degree polynomial (orange curve) to highlight mode-dependent PA trends.



(b) Ellipticity angle (EA) profiles for drift modes A0 (black) and B (green) as a function of pulse longitude.

Figure 3.31: Comparison of position and ellipticity angle profiles for drift modes A0 and B.

Chapter 4

Discussion

We conducted a detailed investigation of the polarization characteristics of remarkable subpulse drifting phenomenon seen in the pulsar PSR J0026–1955. We performed two sets of observations for this source, using the uGMRT's superior sensitivity and wide-band capabilities. Our analysis identified four distinct drift modes as well as significant nulling.

Our recent observations in polarimetric analysis of polarisation profiles reveal that circular polarization dominates over linear polarization within the pulse window. This behavior may be attributed to polarization leakage arising from polarimetric calibration inaccuracies in the instrument. The integrated pulse profile for cycle 41 (Figure 3.2) shows negative circular polarization (V), while cycle 47 (Figure 3.3) shows positive V. A long-term observational study of how the handedness of V evolves could be valuable for future research.

We conducted the first polarimetric study of both stable and evolutionary subpulse drifting modes of this pulsar. We constructed the subpulse drifting single pulse stacks in all four Stokes modes and examined the resultant evolution of the derived polarimetric parameters like the ellipticity angle, position angle, polarization degree, etc. All four Stokes parameters exhibit drift-synchronous modulation across all drift modes. On a longer time scale, the circular polarization appears to be the most prominent near the central longitude of the pulse stack. We find periodic changes in circular polarization across the pulse stack by analyzing the pulse sequences in Stokes I, Q, U, and V (3.18, 3.19, 3.20, and 3.21). This kind of analysis is rarely done, and only a few studies have looked at circular polarization in this way, making our result a notable contribution. The periodicities in the circular polarisation (V)

observed along the drift bands may be explained by a combination of intrinsic emission structure and coherent emission processes. If the pulsar emission arises from a system of discrete subbeams circulating around the magnetic axis (the "carousel" model), periodic V patterns could occur if the same subbeam, associated with a fixed handedness of circular polarisation, repeatedly crosses our line of sight in a regular manner. This would naturally produce periodic variations in V along the drift bands. Additionally, coherent radiation mechanisms, such as curvature radiation by bunches of charges, often generate strong and structured polarisation. If these particle bunches preferentially emit with a specific circular polarisation handedness, their periodic appearance during the drift could further reinforce the observed repeating V signatures.

As discussed earlier, we also identified distinct drift features in the Stokes parameters. Notably, the drift bands appear to retain polarisation information even after nulls. In Figures 3.24 and 3.25, changes in the handedness of fractional circular polarization are visible in modes A1 and A2. However, we do not observe any significant periodic changes in handedness for mode A0. In contrast, mode B exhibits considerable switching in the handedness of circular polarization.

Across all modes, the position angle transitions gradually from negative to positive values, starting from earlier to later longitudes. While this variation can be described by the Rotating Vector Model (RVM), the drift-synchronous modulation of the position angle poses a challenge for a satisfactory explanation within the RVM framework. Figure 3.31a shows a sharp transition in the position angle of B compared to the position angle of A0. Earlier studies by Smits, Mitra, and Kuijpers 2005 suggested that modes with smaller P_3 , typically classified as B modes, are formed closer to the magnetic axis compared to A modes, which are believed to originate farther from the magnetic axis. Our investigation of the stable A0 and B modes supports this notion. We found that the averaged position angle variations within the pulse window show that the position angle of B modes changes more rapidly than that of A modes along the longitude, indicating their proximity to the magnetic axis. Additionally, the averaged ellipticity angle variation across the pulse window for both B and A modes reveals that the circular polarization components are stronger (demonstrating more circular behavior) in B modes than in A modes. This suggests that modes forming closer to the magnetic axis exhibit more circular behavior, while the beams that diverge farther away, as seen in A modes, show reduced circularity.

No jumps in the PA curve were observed, indicating a lack of orthogonal polarisation mode (OPM) switching during the observation. In typical cases, OPM switching manifests as abrupt 90° shifts in the position angle, corresponding to transitions between two orthogonal polarisation states. The smoothness of the PA curve suggests a stable polarisation mode throughout the pulse sequence. This implies that a single mode dominates the emission or that any mode switching is too weak to be detected.

In Figure 3.10, we observe abrupt breaks that indicate rapid mode changes. The drift rate (Figure 3.11) primarily shows positive or negative slopes, suggesting that there are more A1 and A2 modes present compared to A0 and B modes. However, it is noted that these A1 and A2 modes do not last for a long duration in terms of pulse numbers.

Chapter 5

Future directions

- A **Poincaré sphere analysis** can be performed to investigate the evolution of polarization states across different drift modes.
 - The Poincaré sphere is a geometrical representation where each point corresponds to a unique polarization state—linear, circular, or elliptical—allowing for intuitive visualization of polarization variations across pulse longitude or time.
 - This method will help uncover mode-dependent polarization signatures and improve our understanding of the emission geometry.
- **Instrumental calibration procedures** can be refined to minimize polarization leakage.
 - Accurate calibration is essential for reliable measurement of Stokes parameters (I, Q, U, V), especially when interpreting small variations in polarization across drift modes or frequencies.
- A **frequency-dependent study** will be conducted to examine how polarization and drifting behavior vary with observing frequency.
 - This will help explore how emission height and beam geometry change across the magnetosphere, and reveal modespecific propagation effects.
 - Wide-band observations from the Square Kilometre Array (SKA) will enable simultaneous tracking of drift patterns across a broad frequency range, offering detailed insight into frequency-dependent emission processes.

- However, the 300–500 MHz Band 3 range of the uGMRT may be insufficient for this analysis, as sub-bandifying the 200 MHz bandwidth would significantly reduce signal-to-noise ratio (SNR), limiting resolution of drift behavior across frequencies.
- The long-term evolution of circular polarization (Stokes V) will be studied to understand temporal changes in the pulsar magnetosphere.
 - Variations in the handedness of V over time may indicate evolving magnetospheric conditions or emission geometry, providing insight into dynamic processes affecting the pulsar's polarization signatures.

Bibliography

- [1] NDR Bhat et al. "The Southern-sky MWA Rapid Two-metre (SMART) pulsar survey—I. Survey design and processing pipeline". In: *Publications of the Astronomical Society of Australia* 40 (2023), e021.
- [2] FD Drake and HD Craft. "Second periodic pulsation in pulsars". In: *Nature* 220.5164 (1968), pp. 231–235.
- [3] Russell T Edwards. "The polarization of drifting subpulses". In: *Astronomy & Astrophysics* 426.2 (2004), pp. 677–686.
- [4] Thomas Gold. "Rotating neutron stars and the nature of pulsars". In: *Nature* 221.5175 (1969), pp. 25–27.
- [5] Peter Goldreich and William H. Julian. "Pulsar Electrodynamics".
 In: *The Astrophysical Journal* 157 (Aug. 1969), p. 869. DOI: 10. 1086/150119.
- [6] Yashwant Gupta et al. "The upgraded GMRT: opening new windows on the radio Universe". In: *Current Science* (2017), pp. 707–714.
- [7] A. Hewish et al. "Observation of a Rapidly Pulsating Radio Source". In: *Nature* 217.5130 (Feb. 1968), pp. 709–713. DOI: 10.1038/217709a0.
- [8] Parul Janagal et al. "PSR J0026- 1955: A curious case of evolutionary subpulse drifting and nulling". In: *Monthly Notices of the Royal Astronomical Society* 524.2 (2023), pp. 2684–2697.
- [9] Sanjay Kudale et al. "In-field Phasing at the Upgraded GMRT". In: *The Astrophysical Journal* 972.1 (2024), p. 61.

- [10] Samuel J McSweeney et al. "Independent Discovery of a Nulling Pulsar with Unusual Subpulse Drifting Properties with the Murchison Widefield Array". In: *The Astrophysical Journal* 933.2 (2022), p. 210.
- [11] SJ McSweeney et al. "Low-frequency Observations of the Subpulse Drifter PSR J0034- 0721 with the Murchison Widefield Array". In: *The Astrophysical Journal* 836.2 (2017), p. 224.
- [12] LS Oswald, Aris Karastergiou, and Simon Johnston. "Pulsar polarization: a partial-coherence model". In: *Monthly Notices of the Royal Astronomical Society* 525.1 (2023), pp. 840–853.
- [13] N Primak et al. "The polarisation of the drifting sub-pulses from PSR B1919+21". In: *Astronomy & Astrophysics* 657 (2022), A34.
- [14] N. Primak et al. "A&A". In: A&A 657 (2022), A34.
- [15] V Radhakrishnan and DJ Cooke. "Magnetic poles and the polarization structure of pulsar radiation". In: (1969).
- [16] R Ramachandran et al. "Pulsar "drifting"-subpulse polarization: No evidence for systematic polarization-angle rotations". In: *Astronomy & Astrophysics* 381.3 (2002), pp. 993–999.
- [17] Joanna M Rankin, Geoffrey AE Wright, and Andrew M Brown. "Drifting, moding and nulling: another look at pulsar B1918+19". In: *Monthly Notices of the Royal Astronomical Society* 433.1 (2013), pp. 445–456.
- [18] Suda Harshavardhan Reddy et al. "A wideband digital back-end for the upgraded GMRT". In: *Journal of Astronomical Instrumentation* 6.01 (2017), p. 1641011.
- [19] MA Ruderman. "P. G. Sutherland". In: Ap. J. 196 51 (1975).
- [20] JM Smits, D Mitra, and J Kuijpers. "Frequency dependence of the drifting subpulses of PSR B0031-07". In: *Astronomy & Astrophysics* 440.2 (2005), pp. 683–692.
- [21] K Stovall et al. "The green bank northern celestial cap pulsar survey. I. Survey description, data analysis, and initial results". In: *The Astrophysical Journal* 791.1 (2014), p. 67.